Alma Mater Studiorum · Università di Bologna

Scuola di Scienze
Dipartimento di Fisica e Astronomia
Corso di Laurea in Fisica

Preparation and commissioning of a laser setup for characterisation of the ePIC-dRICH silicon photomultipliers at the EIC

Relatore:
Prof.ssa Gilda Scioli

Correlatore:
Dott. Roberto Preghenella

Presentata da:
Arnaldo Bartoli

Anno Accademico 2022/2023

Sommario

Il futuro acceleratore di particelle EIC (Electron Ion Collider) approfondirà le nostre conoscenze riguardo l'interazione forte, analizzando collisioni di elettroni con nuclei e protoni. Il rivelatore dell'esperimento ePIC presso EIC prevede un sistema d'identificazione di particelle, per il quale è stato preso in considerazione il rivelatore dual-radiator RICH. Quest'ultimo impiega due radiatori e integrerà appositi fotosensori per rilevare l'emissione di luce Cherenkov e risalire alla massa delle particelle. I sensori al silicio SiPM sono i principali candidati come fotorivelatori.
L'obiettivo di questo lavoro di tesi è la preparazione, la messa in funzione e la caratterizzazione di un set-up sperimentale per lo studio della risposta di sensori SiPM, tenuti a basse temperature. In particolare, l'attività si concentra sulla caratterizzazione del laser utilizzato per illuminare i SiPM.
Un aspetto rilevante emerso dall'analisi dati è che, utilizzando il laser in modalità pulsata, la potenza del laser aumenta in modo non lineare rispetto alla frequenza degli impulsi, suggerendo che le prestazioni del sistema dipendano dalla frequenza degli impulsi del laser.

Abstract

The future EIC (Electron-Ion Collider) particle accelerator will deepen our knowledge on the strong interaction, by analyzing collisions of electrons with nuclei and protons. The particle detector for the ePIC experiment at the EIC includes a particle identification system, for which the dual-radiator RICH detector has been taken into consideration. The latter employs two radiators and will integrate specific photosensors to detect the emission of Cherenkov light and trace the mass of the particles. SiPM silicon sensors are prime candidates as photodetectors.

The objective of this thesis work is the preparation, commissioning and characterization of an experimental set-up for the study of light response of SiPM sensors, kept at low temperatures. Specifically, the activity focuses on the characterization of the laser used to illuminate SiPMs.

One relevant aspect that emerged from data analysis is that, by using the laser in pulsed mode, the laser power increases non-linearly with respect to the pulse frequency, suggesting that the performance of the system does depend on the laser pulse rate.

Contents

Introduction **3**

1 The Electron Ion Collider **5**
1.1 Analysis objectives . . . 5
1.1.1 Proton spin . . . 6
1.1.2 Proton tomography . . . 6
1.1.3 Quark hadronization . . . 7
1.1.4 Gluons saturation . . . 8
1.2 The EIC infrastructure . . . 8
1.2.1 Detectors . . . 10
1.2.2 Particle identification: Cherenkov radiation . . . 11

2 Silicon Detectors **13**
2.1 Semiconductors and p-n junction . . . 13
2.2 The SiPM . . . 15
2.2.1 Structure: SPAD and quenching circuit . . . 15
2.2.2 Photon Detection Efficiency . . . 17
2.2.3 Noise . . . 18
2.2.4 Radiation damage and annealing . . . 20

3 Set-up and laser characterization **23**
3.1 The set-up . . . 23
3.1.1 Inside the climatic chamber . . . 23
3.1.2 Mounting the rack . . . 24
3.1.3 Optical components . . . 26
3.2 Pulse generator and signals synchronization . . . 29
3.2.1 Checking signals synchronization . . . 29
3.2.2 Checking signals jitter . . . 31
3.3 Laser characterization . . . 33
3.3.1 Checking laser light intensity . . . 34
3.3.2 Noise at room temperature . . . 35

3.3.3 Detection rate and probability 36
3.3.4 Frequency scan 37
3.3.5 Detection rate and laser power 40
3.3.6 Threshold scan 45
3.3.7 Changing the light collimator 50
3.3.8 Faraday cage for the laser 52
3.4 Final system characterization 53

Conclusions **57**

Introduction

The Electron-Ion Collider (EIC) particle accelerator will be built in the USA during this decade, with the aim of investigating nuclear structure and nuclear strong interaction. Design projects for the detector[1] involve three major systems: one for tracking and vertexing, one for particle identification and another for calorimetry. For particle identification, the dual-radiator Ring Imaging CHerenkov (dRICH) detector is one the main components in the forward region. This detector will involve the use of photosensors, in order to detect Cherenkov radiation from particles and determine their mass. Currently, SiPM silicon detectors are being considered for this purpose, because of their constained dimensions and single-photon detection capability.
This work is focused on the characterization of a set-up that will be used to study the light response of SiPM sensors. The set-up includes a laser light source that can be operated from remote, in order to illuminate SiPMs that are kept at low temperature, so as to limit thermal noise.

Chapter 1 gives an overview on the Electron-Ion Collider, presenting the main goals it aims to achieve and describing some of the designs currently under consideration for detectors, specifically for particle identification.

Chapter 2 introduces the basic functioning principle of silicon detectors: the p-n junction. Also, the chapter delves into SiPM sensors, presenting their structure, characteristics, possible noise sources, as well as some of the tecniques used to restore their performance after radiation damage.

Chapter 3 describes the set-up arranged for this work, from its proper building to the measurements carried out in order to characterise the light source and the results emerged from the analysis of signals from SiPMs.

[1]The particle detector currently considered for the EIC is the ePIC (electron-Proton/Ion Collider) detector.

Chapter 1

The Electron Ion Collider

The Electron-Ion Collider (EIC) is an upcoming particle accelerator and collider, that will be built over the next ten years at the Brookhaven National Laboratory (BNL), in the USA. The EIC is designed to collide high-instensity polarized electron beams with polarized beams of protons, light ions and heavier ions, up to Uranium ones [1].
Equipped with large detectors, the future set-up is expected to provide precise measurements that will allow us to have a better understanding of nuclear structure and nuclear strong force, that is, quarks and gluons that form matter. In fact, quarks and gluons, collectively called partons, are the fundamental constituents of nucleons. Also, gluons are the mediating particles for strong interaction between quarks. The Quantum Chromo-Dynamics (QCD) theory has partons as object of interest and attributes the strong force between quarks and gluons to their color charge, which is also responsible for interaction between gluons themselves.
The EIC will investigate how the nucleon mass and spin arise from the ones of their constituents, as well as the distribution of momenta and position of partons inside the nucleon and the properties of dense gluon systems. All of these subjects will be studied in one single facility, thanks to the wide range of kinematic, beam polarization and beam species, specific to the EIC [2].

Section 1.1 introduces the main nuclear properties and structures that EIC analyses will address.
Section 1.2 reports the proposed layout and requirements for accelerator and detectors.

1.1 Analysis objectives

The strong interaction generates a significant fraction of the nucleon mass and binds partons so that the internal structure of nucleons can be investigated only when they collide at high speed. A deeper understanding of this regime will require the higher energy and beam polarization of the Electron-Ion Collider.
In specific, the EIC is designed to facilitate mapping of distribution of nucleon partons,

spin, flavour and momentum, including its transversal component.

1.1.1 Proton spin

Compared to current data collected from high energy experiments, the EIC will allow to reach two orders of magnitude lower in the minimum accessible momentum fraction (x) and to span a wider range of momentum transfer (Q). This would allow to lower measurement uncertainties (Figure 1.1) and precisely quantify the contribution of the spin of quarks and gluons to that of hadrons, specifically the proton.

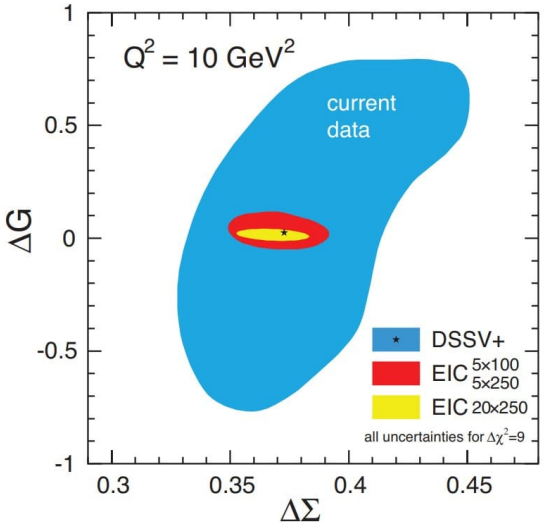

Figure 1.1: Projected reduction in the uncertainties of the gluon's helicity (projection of spin onto the direction of momentum) contribution (ΔG) vs the quark helicity contribution ($\Delta\Sigma$) from the region of parton momentum fraction $x > 0.001$, that would be achieved by the EIC for different center-of-mass energies [1].

As a matter of fact, quarks are responsible only for 30% of total proton spin. The spin of gluons, while it does contribute, can't make up for the remaining 70%. But it is known that gluons can split into virtual quark-antiquark couples, that eventually recombine into new gluons. Quarks forming virtual couples are called "sea quarks". The EIC is going to extend our knowledge also on the role of sea quarks in determining proton structure and spin.

1.1.2 Proton tomography

The motion and the spin of partons are correlated to Transversal Momentum dependent parton Distributions (TMDs). So, by investigating on electron and nucleon polarized

beams collisions, TMDs can reveal some new information about the motion of gluons and sea quarks confined inside fast-moving nucleons.
Also, by probing the transversal spatial distribution of partons as a function of their longitudinal momentum fraction, the EIC will provide an image of the proton that is complementary to the one obtained from the transverse momentum distribution.
This way, it will be possible to create a tomographic image of the proton, more precise on the transversal distances than any other existing facility. This imaging technique contains information about spin-orbit correlations and about the angular momentum, spin and orbital motion of partons.

1.1.3 Quark hadronization

The EIC will provide a wide variety of ion beams for electron-nucleus collisions, that can give insights on how quarks and gluons lose energy and hadronize in cold nuclear matter. In fact, a virtual photon generated in a scattering event may interact with a quark from a nucleon, giving this latter enough energy to move inside a nucleus, interacting with its other constituents. The end product of this interaction would be the production of a colorless hadron. Figure 1.2 gives a schematic representation of this process.

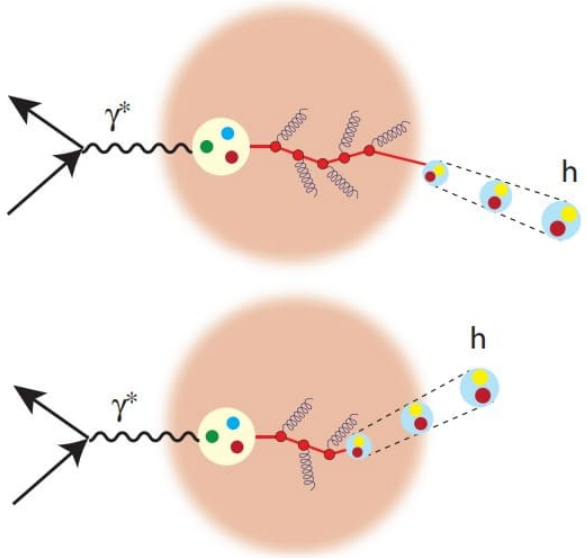

Figure 1.2: Diagram of a parton moving inside a nucleus in cold QCD matter; final hadron can be produced outside (top) or inside (bottom) the nucleus [1].

1.1.4 Gluons saturation

Thanks to the EIC, a new state of nuclear matter is expected to be observed: the Color Glass Condensate (CGC). The word "color" refers to the charge carried by gluons, "glass" represents disordered elements changing their positions, and "condensate" refers to the elevated density of the state.
Gluon density is regulated by a non-linear process of gluon splitting and gluon-gluon recombination. When these two processes reach a balance, density reaches a dynamic saturation scale at which new properties of hadronic matter would emerge.
This saturation scale will be more accessible thanks to the EIC heavy ion collisions, since the big number of quarks involved in the process results in a decrease of the needed energy, as shown in Figure 1.3.

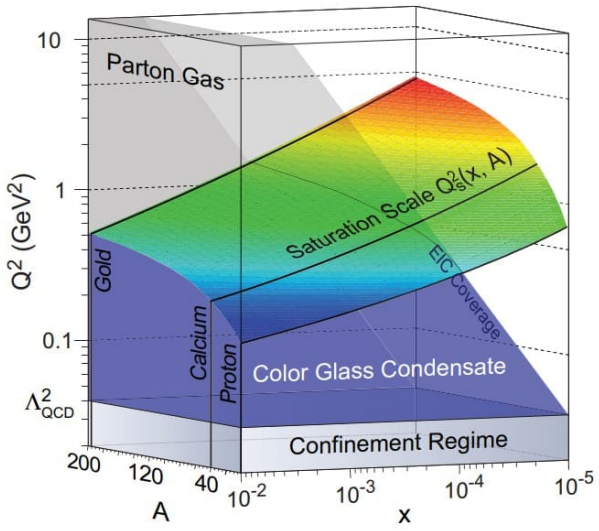

Figure 1.3: Theoretical expectations for the dependence of the saturation scale on the nuclear mass number A, the minimum momentum fraction x and momentum transfer Q [1].

1.2 The EIC infrastructure

The EIC infrastructure projects (Figure 1.4) are based on the already existing Relativistic Heavy Ion Collider (RHIC), at the Brookhaven Nation Laboratory. The new accelerator aims to achieve the following features:

- highly polarized beams of electrons and nuclei;

- beams of ions from particles, that range from deuterons to heavy nuclei;
- a center-of-mass energy that varies in the range ∼20÷100 GeV, upgradable to ∼140 GeV;
- high particle collision rate, with a luminosity in the range $\sim 10^{33} \div 10^{34}\ cm^{-2}s^{-1}$;
- multiple interaction regions, with at least one detector.

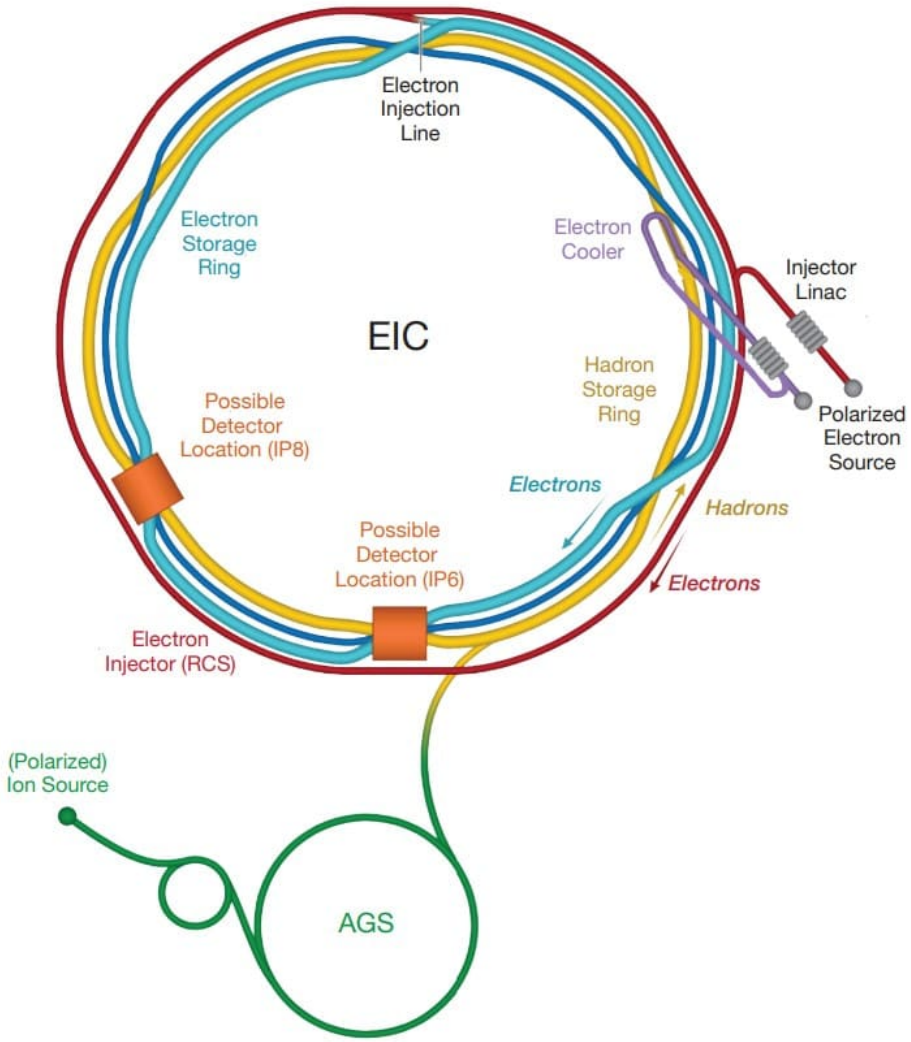

Figure 1.4: Diagram of the EIC accelerator, based on the existing RHIC infrastructure at Brookhaven National Laboratory [2].

1.2.1 Detectors

Detectors located at interaction regions will provide precise energy measurements, particle tracking and particle identification, in order to fully characterize the four-vector of each particle involved in electron-ion collisions. Current detector designs, as the one studied in detail by the ATHENA proto-collaboration [3] and now adopted by the established ePIC Collaboration at the EIC, are centered around a solenoidal superconductive magnet and therefore the various detection systems will be arranged in a "barrels and endcaps" configuration.

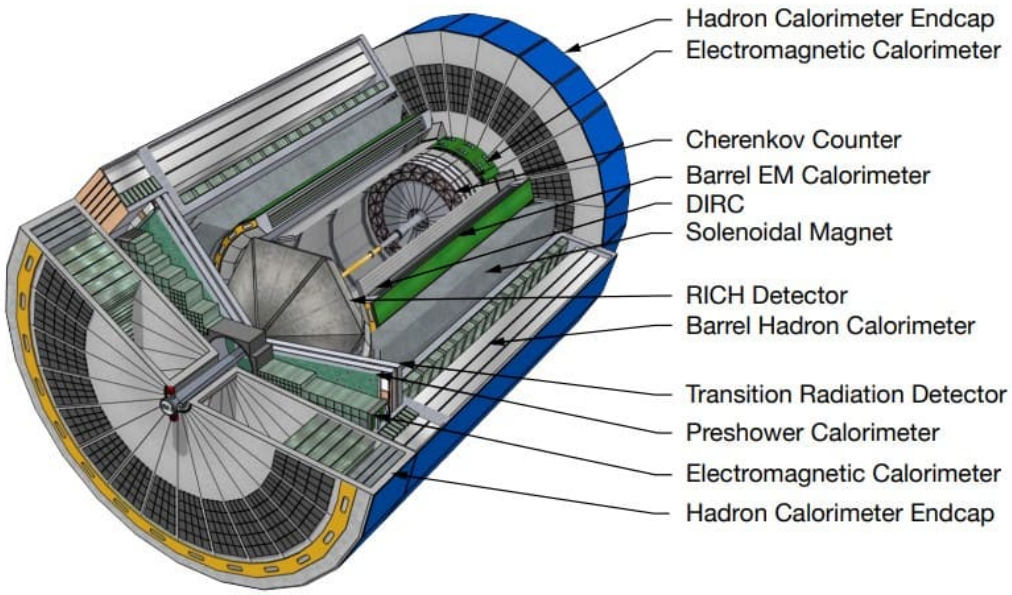

Figure 1.5: CAD model of a EIC detector concept, with subsystems for tracking, particle identification, and calorimetry [2].

Taking into account the wide variety of particles the experiments will focus on, as well as the asymmetry of collisions, the aim is to combine complementary detector technologies and concepts to achieve the full set of requirements, depending on the interaction region they are located at.
According to Figure 1.5, the following main systems of the detectors can be identified:

- an innermost system for particle tracking and vertexing; silicon-based semiconductors collect electron/hole pairs caused by the passage of charged particles, while gas-based tracking technologies collect ionization caused by tracks;
- a system for particle identification, which exploits time of flight measurements and Cherenkov light emission (Paragraph 1.2.2);

- an outermost system that measures energy for both electrons and hadrons, thanks to an electromagnetic calorimeter and a hadron calorimeter; due to the limited space, currently, SiPM sensors are favoured for these measurements, since they take less space and can operate in the magnetic field.

1.2.2 Particle identification: Cherenkov radiation

Particle identification deserves a deeper description. It uses detectors based on Cherenkov radiation, as well as on time-of-flight technique. We focus here on the Cherenkov identification technique.
Cherenkov radiation is emitted by a charged particle that moves through a dielectric medium with a speed greater than light's phase velocity in that medium. The angle θ at which light is emitted is then related to the particle's speed v:

$$cos(\theta) = \frac{1}{n\beta}; \tag{1.1}$$

where n is the refraction index of the medium and $\beta = v/c$, where c is the speed of light in vacuum.
It follows, from equation 1.1, that a measure of θ results in a measure of v. By combining this information with the one on momentum, it is then possible to determine the particle's mass and identify it. We can then observe how Cherenkov light emission only occurs when the particle's speed is greater than the light's speed in the medium:

$$|cos(\theta)| \leq 1 \Rightarrow |\frac{1}{n\beta}| \leq 1 \Rightarrow v \geq \frac{c}{n}. \tag{1.2}$$

Among the proposed options for Cherenkov detectors, the dual Ring-Imaging CHerenkov detector (dRICH) is significant (Figure 1.6). The device is composed by two different radiators, which have two different refraction indexes (n): an aerogel radiator, with $n = 1.02$ and a gas radiator, with $n = 1.0008$. The dRICH detector will also implement highly segmented photosensors and, as for calorimetry, SiPM sensors are currently selected for the readout in this region of the detector.

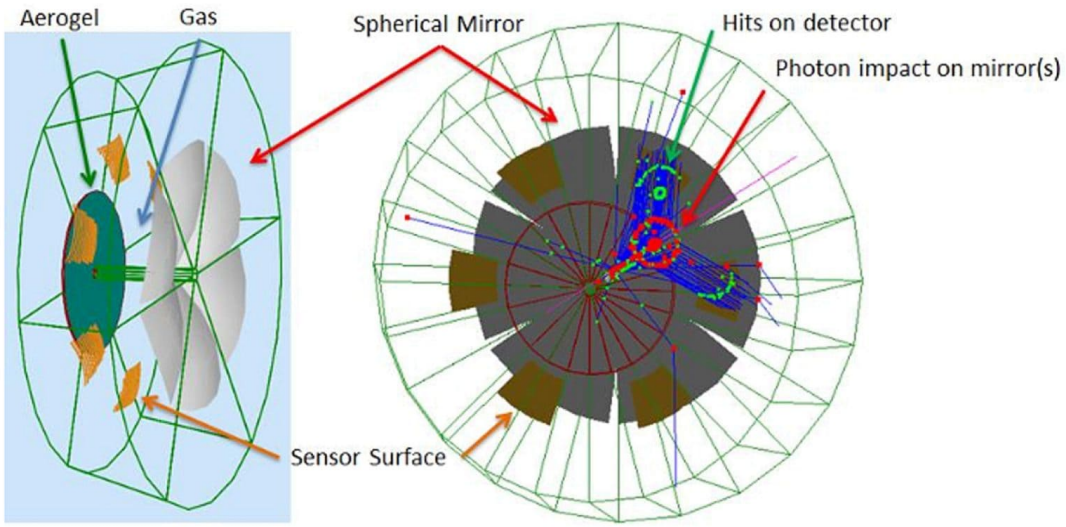

Figure 1.6: Dual RICH detector configuration [2].

Chapter 2

Silicon Detectors

Semiconductor detectors are widely used in high-energy physics for charged particles and photons detection. SiPM sensors are semiconductor detectors based on silicon and, as mentioned in Section 1.2, they are being considered for calorimetry and particle identification for the EIC. Also, SiPMs have been paramount for this work. Section 2.1 introduces the basics of common semiconductor detectors, while Section 2.2 analyzes the main features of SiPM sensors.

2.1 Semiconductors and p-n junction

Semiconductor materials used in solid-state detectors are made up of elements from the IV group of the periodic table. The atoms are organized in a crystal lattice, so that their electronic energy levels merge into two bands: a valence band and a conduction band, separeted by an energy gap, typically about 1 eV (Figure 2.1, left).

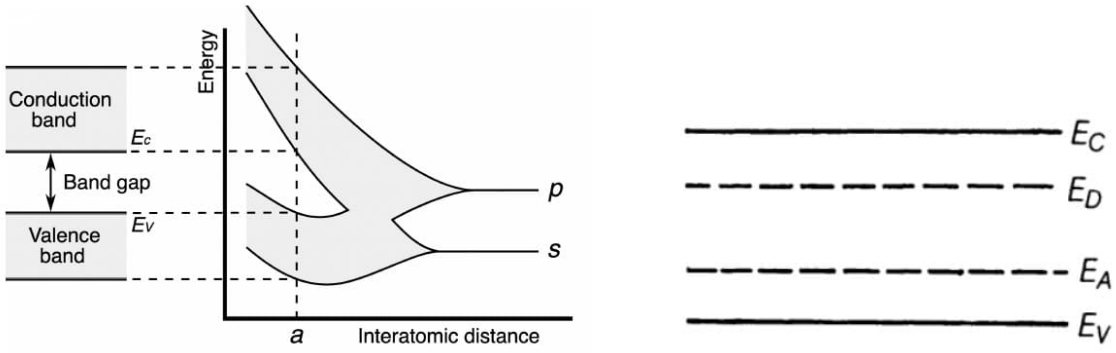

Figure 2.1: Emergence of bands structure at low interatomic distances (left); diagram of electron energy levels in a crystal lattice (right), in ascending order from bottom to top, where E_V and E_C are respectively the edges of valence and conduction bands, while E_A and E_D are the acceptor and donor levels [4].

Valence band houses electrons forming covalent bonds between atoms, while conduction band houses electrons free to move through the lattice, thus able to conduct electrical current. It is possible to substitute some of the atoms in the lattice with others from groups III and V, that have different valence electron number. This process is called doping. Atoms of the V group[1] act as "donors" of extra electrons, that may then conduct electricity. Atoms of the III group[2] make "holes" (lack of electron) available, acting as "acceptors" of electrons. The presence of impurities within the crystal corresponds to an additional energy level inside the gap between valence and conduction band, as shown in Figure 2.1 (right).

Materials doped with elements of groups III and V are respectively called p-type and n-type semiconductors. The interface between a semiconductor of one type and one of the other forms the p-n junction, that conducts electrical current primarily in one direction. Silicon detectors usually consist of diodes, that are based on p-n junctions.
So, there's a gradient between primary charge carriers one side of the interface and the other: holes (positive) in the p-doped region and electrons (negative) in the n-doped region. This gradient forces charges to move from one side of the junction to the other, so that in proximity of the inteface charges of opposite signs neutralize themselves, depleting mobile charges inside what is called "depletion region". This process continues, giving rise at the same time to an electric field that opposes the diffusion motion, until an equilibrium is reached. Figure 2.2 (left) shows a schematic representation of the p-n junctioin.

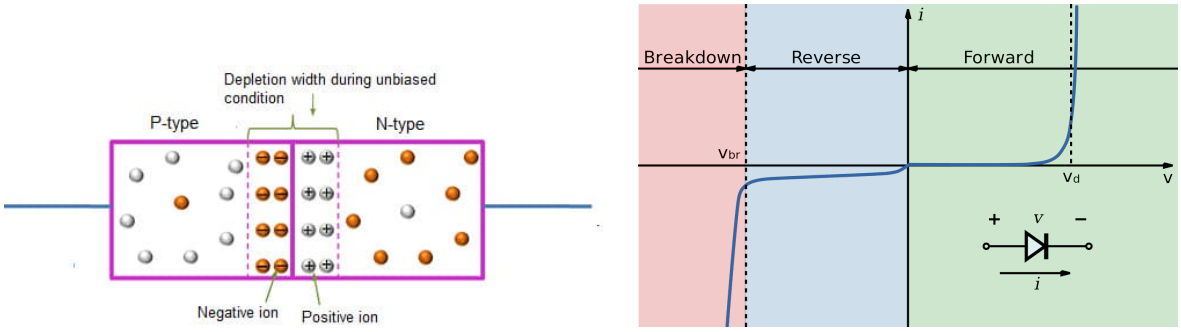

Figure 2.2: Diagram of a p-n junction (left); characteristic curve of a p-n junction (right), where V_d is the threshold voltage and V_{bd} the breakdown voltage.

A p-n junction operates in two main regimes: forward bias and reverse bias. Froward bias configuration is realized by connecting the p-type region to the positive electrode of the voltage source, while reverse bias sees the same p-type region attached to the

[1]Phosphorus (P), arsenic (As) and antimony (Sb) are typycal group V elements used in doped semiconductors.

[2]Boron (B) and Aluminium (Al) are typycal group III elements used in doped semiconductors.

negative electrode.
In forward bias, the junction conducts electrical current, that increases exponentially with respect to applied voltage from a certain threshold voltage value V_d, as shown in Figure 2.2 (right). In reverse bias, the p-n junction behaves approximatively as an open switch. In fact, in this configuration, the width of the depletion region increases with respect to the unbiased condition and at the same time, the barrier potential across the junction increases, preventing flow of primary charges. If the applied reverse voltage increases over the breakdown voltage V_{bd}, the electric field reaches a critical level at which it breaks down the dielectric, causing an extreme current increase.
Usually, silicon detectors are operated in reverse bias. When an energetic particle travels through the detector it can generate an electron-hole pair which, under the influence of the depletion region's electric field, travels to the electrodes resulting in a measurable current.

2.2 The SiPM

The Silicon PhotoMultiplier (SiPM) is an array of independent microcells, consisting each of a SPAD sensor and a quenching circuit.

2.2.1 Structure: SPAD and quenching circuit

Single Photon Avalanche Diodes (SPADs) are photodiodes whose contained dimensions allow for signle-photon detection resolution. Usually, a SiPM measures few millimeters and it integrates a series of parallel-connected microcells each containing a SPAD, whose size varies typically between 20x20 μm and 50x50 μm. Figure 2.3 shows the structure of an analog SiPM [8].

If the electric field in the SPAD's depletion region is intense enough, when a charge carrier is generated it gains enough kinetic energy to create secondary electron-hole pairs through a process called "impact ionization", triggering a self-sustaining avalanche process, that results in a macroscopic current flow. This process is called Geiger discharge.
High electric field is reached by applying a bias voltage V_{bias} greater than the nominal breakdown voltage of the diode. This way, the flow of current does not stop unless voltage is lowered below the breakdown value. This is done by the quenching circuit.
Then, the diode recharges back to the bias voltage and it is again able to detect photons. The voltage across the diode returns to the nominal value in a time interval called "recovery time". This cycle is represented in Figure 2.4 (left).
The difference between the bias voltage value and the breakdown point is called "over-voltage". As the breakdown voltage is linearly correlated to temperature, also the over-voltage will have a linear dependence from temperature, as shown in Figure 2.4 (right).

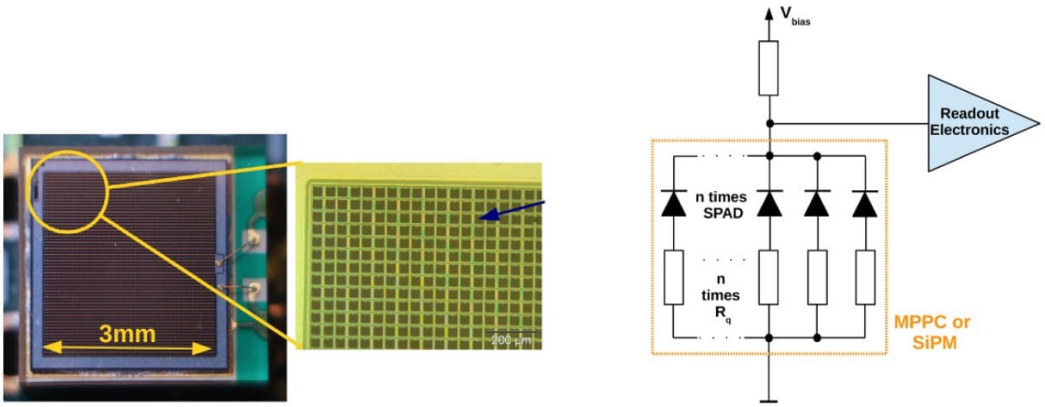

Figure 2.3: (a) Picture of an analog SiPM, with zoom on the individual SPADs (indicated by the arrow); (b) all SPADs with integrated quenching resistor are connected in parallel [8].

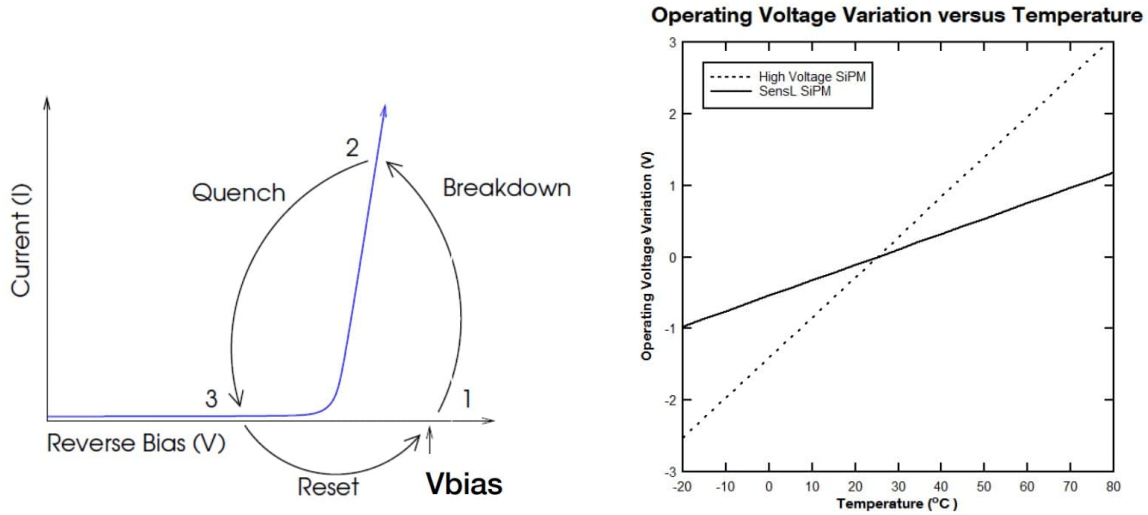

Figure 2.4: On the left, current as a function of applied voltage, with breakdown, quench and reset cycle [6]; On the right, overvoltage ("Operating Voltage") as function of temperature [6].

This relation is relevant for large temperature fluctuations.

A typical SiPM output pulse is shown in Figure 2.5 (left). The rise time of the pulse is determined by the avalanche formation as well as by the output impedance of the sensor. The recovery time of the sensor, i.e. the decay time of the pulse, depends on the microcell

recharge time constant τ_{RC}, given by:

$$\tau_{RC} = C_d(R_q + N \cdot R_s); \tag{2.1}$$

where C_d is the capacitance of the microcell, R_q is the quenching circuit resistance, N is the total number of microcells in the sensor and R_s is any resistance in series with the sensor.
Another relevant parameter for a SPAD is its "gain" (G), that quantifies the number of charge carriers generated per event:

$$G = \frac{C_d \cdot \Delta V}{e}; \tag{2.2}$$

where ΔV is the overvoltage and e the elementary charge.
The microcell can still fire during the recovery time, but the gain will be reduced in proportion to the reduced overvoltage (Figure 2.5, right).

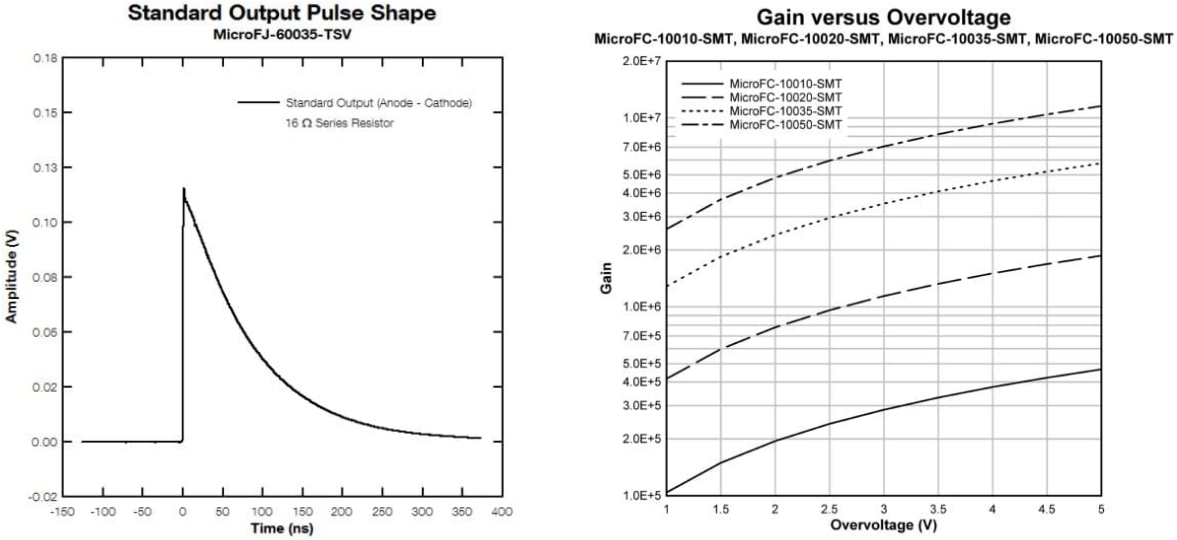

Figure 2.5: Typical output pulse of a SiPM (left) [6]; gain as a function of over-voltage for different microcell size SiPMs (right) [6].

2.2.2 Photon Detection Efficiency

The Photon Detection Efficiency (PDE) of a SiPM measures the sensitivity of the photomultiplier, that is the statistical probability for an impinging photon to interact with

a microcell and generate a detectable signal. PDE depends on the wavelength of the incident light λ and the overvoltage ΔV:

$$PDE(\lambda, \Delta V) = \eta(\lambda) \cdot \epsilon(\Delta V) \cdot F; \tag{2.3}$$

where $\eta(\lambda)$ indicates the "quantum efficiency", that is the probability for an incident photon to generate an electron-hole pair in the sensor, while $\epsilon(\Delta V)$ is the avalanche initiation probability (not every charge may trigger an avalanche). F in Equation 2.3 denotes the so-called "fill factor" of a SPAD, that is the percentage of area of the sensor that's sensitive to light.
PDE is commonly calculated from the responsivity (R) of the sensor, which is defined as the average photocurrent produced per unit optical power [6]. The resulting expression for PDE is:

$$PDE(\lambda, \Delta V) = \frac{R \cdot h \cdot c}{\lambda \cdot e \cdot G \cdot (1 + P_{AP})(1 + P_{XT})}; \tag{2.4}$$

where h is the Planck constant, c is the speed of light in vacuum, e is the elementary charge and G is the gain. P_{AP} and P_{XT} are respectively the afterpulsing and crosstalk probabilities (Paragraph 2.2.3).
Figure 2.6 shows the PDE dependency on the wavelenght of light impacting the sensor, for the specific SiPM sensors used for this work.

2.2.3 Noise

SiPM readout is affected by noise signals, that contribute to the sensor's output signal as shown schematically in Figure 2.7.
The Dark Count Rate (DCR) is the primary source of noise in a SiPM and it is due to thermally-generated electron-hole paris. In fact, when a thermally-generated charge initiates an avalanche, that results in a signal that is indistinguishable from the one produced by an incident photon. As electron-hole pair formation is favoured by a temperature increase, also DCR increases as temperature rises. As Figure 2.8 shows, DCR also increases with the bias voltage at which the sensor is operating, due to the increase in the amount of generated charge carriers.
DCR can be reduced by setting a threshold above the single photon level, but this noise source will still contribute to the measured signal. If signle-photon detection is the goal, as it is for the dRICH detector at the EIC, then it is more appropriate to reduce DCR by operating the sensors at low temperature.

An avalanche in a SPAD produces secondary photons, with wavelength usually in the infrared region and these photons may trigger a new avalanche in a nearby microcell. This phenomenon is named crosstalk and it is a secondary source of noise. As a consequence

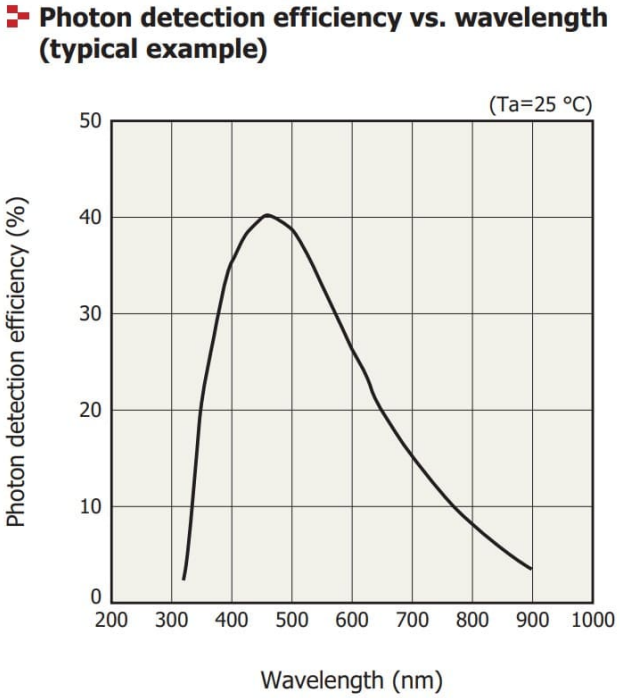

Figure 2.6: Photon detection efficiency as a function of the wavelenght of incident light, for HAMAMATSU S13360 series SiPM sensors (from manufacturer data sheet).

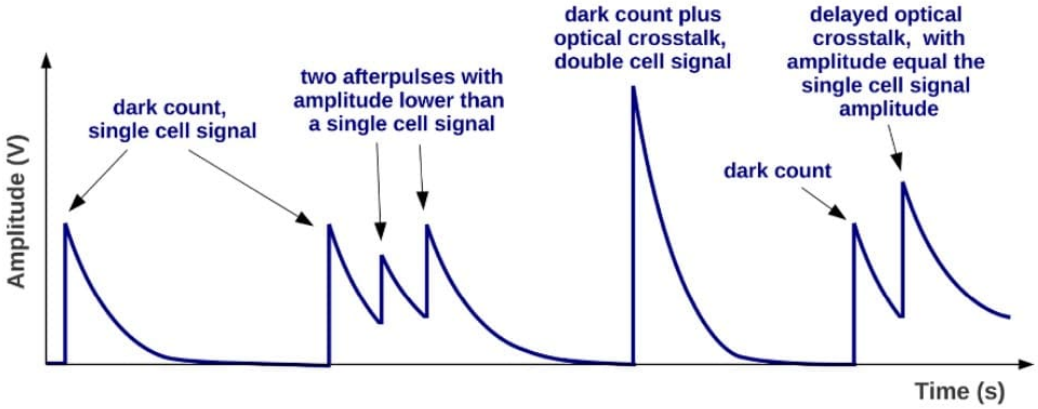

Figure 2.7: Representation of the SiPM output signal for different kinds of noise observable: primary events, crosstalk and afterpulse events [8].

of crosstalk, a single incident photon can generate a signal equivalent to the one produced by more than one photon. Crosstalk increases with overvoltage due to the higher amount of carriers that cross the junction in a SPAD.
Crosstalk between microcells can be minimized using low-gain SPADs, since producing

less charges results in reducing production of secondary photons.

Another secondary source of noise is afterpulse and it mainly occurs when a charge is trapped in a defect of the sensor's silicon crystal. When the charge is finally released, it initiates an avalanche that results in a delayed pulse signal, with amplitude usually lower compared to a pulse from an impinging photon. If the delay is short compared to the recovery time, the afterpulse can be neglected, but it can impact measurements if the rate is high. Afterpulse can also be caused by secondary photons produced in an avalanche.
It is then clear that afterpulse can be reduced by mimimizing defects in the silicon sensors.

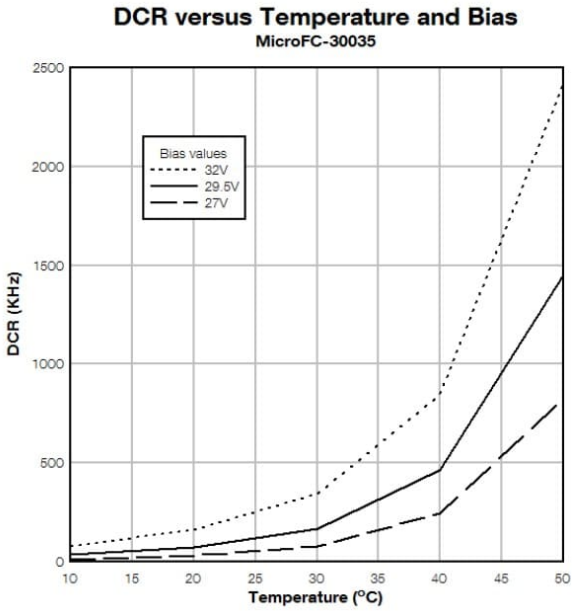

Figure 2.8: Dark count rate (DCR) as a function of operating temperature of the SiPM sensor, for different bias voltage values [6].

2.2.4 Radiation damage and annealing

Silicon crystals in SiPMs can be damaged by particles travelling through. For example, neutrons moving through the silicon can displace some atoms of the lattice, which subsequently form agglomerations called "clusters". Bulk defects from radiation damage result in a deterioration of the sensor's performance, as their presence tends to increase the amount of generated charge carriers and thus the dark current.
SiPM performance can be recovered by thermal annealing, a process consisting in ex-

posing the sensors to high temperatures. The positive effect of thermal annealing on the sensor's performance is shown in Figure 2.9. Annealing can also be electrically induced, either in forward or reverse bias. This tecnique takes advantage of intense electric field generation to re-order the atoms which have been displaced by incoming radiation, providing significant recovery in a relatively small exposure time [12].

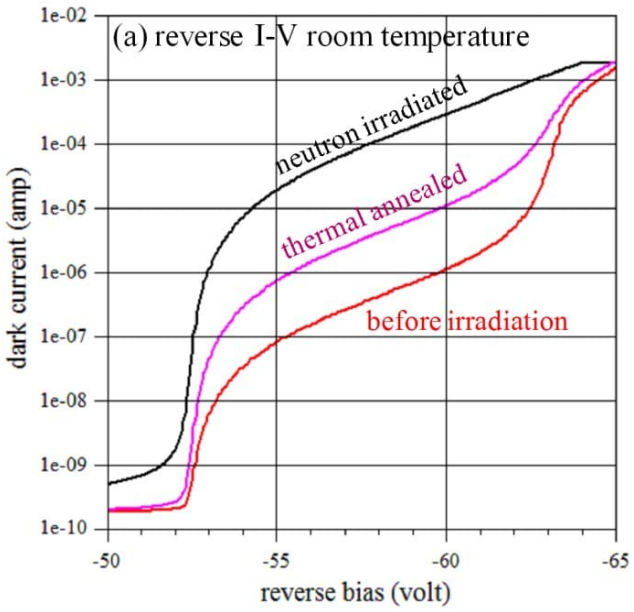

Figure 2.9: Dark current in a SiPM at room temperature, measured before and after irradiation and after a thermal annealing cycle at 250°C [13].

Chapter 3

Set-up and laser characterization

The aim of this work is the implementation and study of a measurement apparatus that incorporates a pulsed laser light source to test the light response of SiPM sensors at low temperature. Section 3.1 describes the building and testing process of the apparatus, while section 3.2 addresses the characterization measurements of the pulse generator used to operate the laser. Section 3.3 presents measurements from the SiPMs response to the laser light, used to fully characterize the laser itself and to check the reliability of its data sheet specifications. Section 3.4 reports definitive signal analysis and time-resolution measurements, from both the laser system and SiPMs.

3.1 The set-up

As the DCR of a SiPM decreases significantly with temperature, the sensors have been kept in a MEMMERT CTC-256 climatic chamber at -30 °C for optimal measurement conditions.
On the other hand, the ALPHALAS laser used to lit the SiPMs is designed to work at room temperature. Therefore a proper rack has been assembled to accomodate the laser as close as possible to the MEMMERT chamber and link the fiber optic cables bringing light from the laser outside the climatic chamber to the inside of this latter, as well as to lodge all the devices needed.

3.1.1 Inside the climatic chamber

As Figure 3.1 and Figure 3.2 show, inside the climatic chamber are installed:

- a support board where the HAMAMATSU SiPM sensors are mounted;
- an X-Y movement system for the support board;
- four ALCOR chips to acquire data from SiPMs;
- four adaper boards to regulate voltage supplied to the SiPMs;

- four Masterlogic boards to interface with the adapter boards;
- a mount-support for the fiber optic cable bringing light from the laser;

The MEMMERT chamber has an aperture on a side, properly designed in order to let cables pass through, connecting components inside and outside, while keeping its interior isolated, maintainig the desired temperature.

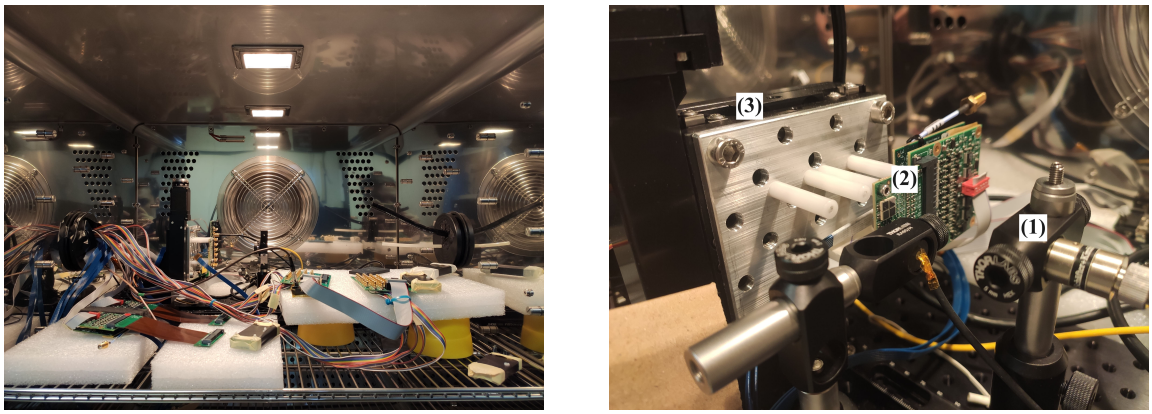

Figure 3.1: Overview on climatic chamber interior (left) and close-up (right) on the optical fiber mount-support (1), the board-mounted SiPMs (2) and the X-Y movement system (3).

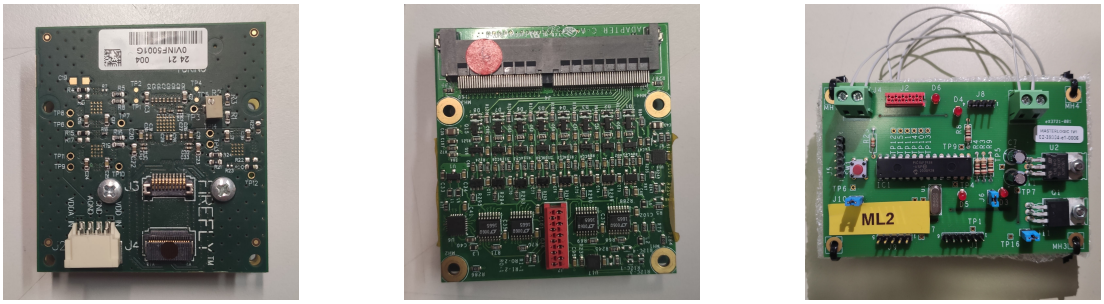

Figure 3.2: Some of the electronic boards used in the set-up; Alcor chip (left), adapter board (center) and Masterlogic board (right).

Also, outside the climatic chamber, a heatless regenerative desiccant dryer KAESER DC 2.0 (Figure 3.3) flows dry air inside the climatic chamber volume.

3.1.2 Mounting the rack

For the rack assembly, suitable shelves have been added to a prebuilt infrastructure using proper screws and tools and optimizing spaces. This in order to house:

Figure 3.3: The KAESER DC 2.0 heatless regenerative desiccant dryer.

- an ALPHALAS Picosecond Diode Laser with Driver PLDD-100M;
- a Thorlabs In-Line Fiber Optic Filter Mount, equipped with a Thorlabs NE50A Absorptive Neutral Density Filter, mounted on a Thorlabs SM1-Threaded Filter Holder;
- a Tektronix AFG3253 function generator;
- an FPGA unit to read data from ALCOR;
- a PLH250-P high voltage supply for SiPM sensors;
- a QL355TP low voltage supply for electronics;
- a KEYTHLEY DAQ6510 multimeter system;
- a KEYTHLEY 2450 multimeter system;
- two Lenovo ThinkCenter PCs and an ethernet hub to give the FPGA unit access to the Internet;

The ALPHALAS laser, shown in Figure 3.4, is provided with a switch that allows choosing to generate a pulsed light signal or a continuous one. We shall refer to these two operating modes as pulser mode and continuous wave mode respectively.
The completed rack, shown in Figure 3.5, has then been placed next to the climatic chamber and a series of three fiber optic cables has been linked from the laser to the inside of the chamber, as described in Paragraph 3.1.3.

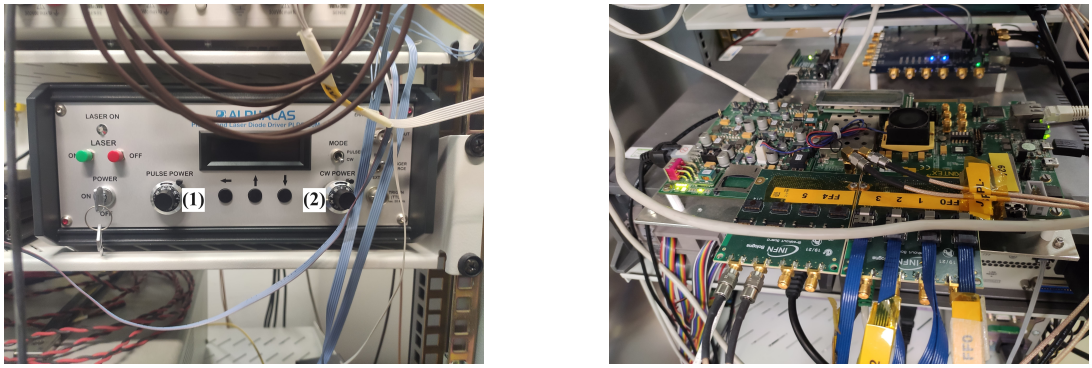

Figure 3.4: Close-up on the ALPHALAS diode laser (left), with knobs regulating its power both in pulser mode (1) and continuous wave mode (2); close-up on the FPGA unit (right).

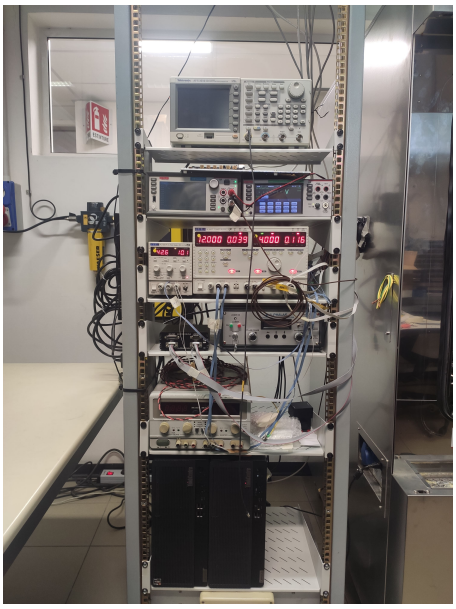

Figure 3.5: Overview on the rack, housing all the electronic devices in their final arrangement.

3.1.3 Optical components

Regulating the intensity of laser light is key to control the rate at which SiPM sensors detect photons. In fact, the laser emits a light beam whose intensity (I) is directly proportional to the numebr of photons emitted per time-unit (N):

$$I = N \cdot E/A; \tag{3.1}$$

where E is the photon energy and A is the light beam cross section area. And we may rewrite the relation considering n photons crossing A in a timespan t:

$$I = n \cdot \frac{E}{At} = n \cdot \frac{P}{A}; \tag{3.2}$$

where $P = E/t$ is the light beam power. Hence, we understand that by managing the light source power we affect the number of photons impacting on our sensors and so the consequent number of photons the sensor is able to see each second.
The laser light power is regulated through dedicated knobs on the device (Figure 3.4). Light intensity is then controlled by implementing attenuation filters along the optic fiber path that light follows (Figure 3.7). This way it is possible to reduce the number of photons impacting the SiPM sensors independently from the laser power knobs. Thorlabs Neutral Density (ND) filters and fiber optic cables serve this purpose.

A fiber optic cable brings light from the laser to the Thorlabs filter mount, from which a series of two other optical fibers, connected to each other, takes light to the inside of the climatic chamber. The one cable that actually enters the climatic chamber is terminated with a light collimator (Figure 3.6, right) that concentrates light in a spot small enough to light a single SiPM sensor.

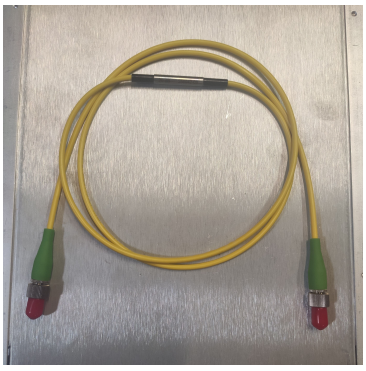

Figure 3.6: One of the three Thorlabs fibers used (left), specifically the one terminated with the collimator (right).

Thorlabs NE50A glass filters measure 25mm in diameter and 3.6mm in thickness and come with a broadband antireflection coating (branded as "A coating") for the 350-700 nm wavelenght range, deposited on both surfaces. This coating is designed to minimize surface reflections, thereby reducing the amount of stray light present. Being optical filters, these devices reduce the intensity of light passing through them. Theoretically, neutral density filters attenuate light intensity without changing its color (hence the term

"neutral"), even though in reality they do at some degree change color rendition [17]. The laser used in this setup emits light at a fixed wavelenght, i.e. with a fixed color, so changes in color rendition are not significant for the outcome of the experiments.

The attenuation ability of a ND filter is quantified by a parameter named "optical density", or "absorbance". The Beer-Lambert Law relates the filter absorbance (A) to the intensity of incoming light (I_0) and the intensity of light exiting the filter (I):

$$A = log(I_0/I); \tag{3.3}$$

where the decimal base logarithm is used.
Thorlabs declares its products absorbance values under the acronym of OD, that stands for optical density. The NE50A filter insered in Thorlabs filter mount (Figure 3.7) has a declared absorbance value of OD = 5.00 ± 0.25. This means that the intensity of the light beam exiting the filter mount is approximately $1/10^5$ of the light beam intensity given directly by the laser.

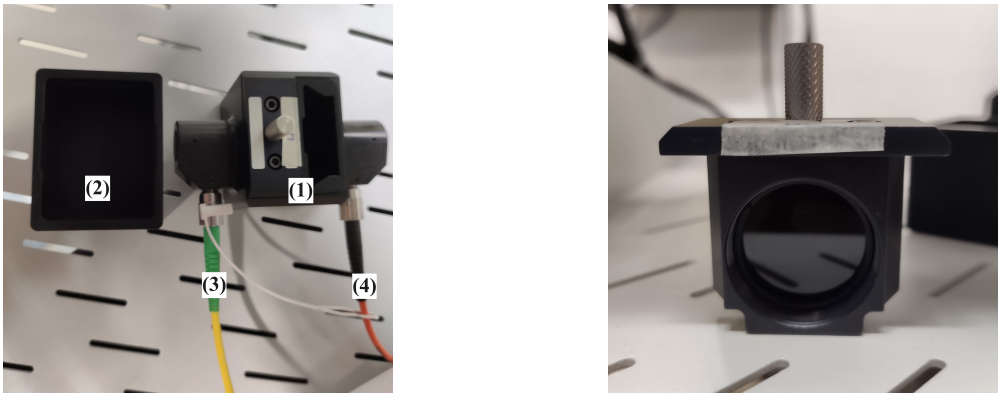

Figure 3.7: On the left, Thorlabs filter mount (1), with its FOFM-CV cover (2), linked to two optical cables: one for incoming light (3) and one for light exiting (4); on the right, the proper attenuation filter (OD = 5.00 ± 0.25), mounted on its holder.

Also, of the three fiber optic cables used, the one terminated with the collimator inside the climatic chamber has an attenuation filter (Figure 3.6, left), that contributes to reduce the light intensity.
The aim is to let just a small amount of light reaching the SiPM sensors, so that they can detect no more than one photon at a time. This aspect will be further investigated in Section 3.3.

3.2 Pulse generator and signals synchronization

Data acquisition from the set-up may be requested at any time and place and may take a significant amount of time, depending on the type of analyses conducted on the SiPM sensors. Therefore, it is desirable for the set-up to be controllable from a remote terminal via Internet. Specifically, it is useful for the laser to be remotely operated, as it is directly resposible for the proper testing of the SiPM sensors. However, the ALPHALAS laser itself is not designed to be operated from remote.

On the other hand, both the Tektronix function generator and the FPGA unit can interface with a remote terminal. Through the function generator it is then possible to set a custom output waveform and operate the laser. Up to this point, the aim would be to link the two devices, in order to organize a chain communication from a remote PC, to the function generator and finally to the laser.
To this purpose, it is necessary to focus on the signals these three components communicate through.

The Tektronix function generator comes with two output terminals, one that generates a NIM signal and one that provides a TTL signal, while the ALPHALAS laser receives in input and generates TTL only. Therefore, in order to control the laser via function generator, the TTL terminal of this latter has been connected to the ALPHALAS device. As the function generator activates and deactivates the laser, i.e. turns it on and off, it is important to keep a record of time-signals corresponding to each activation and therefore the NIM output on the Tektronix device has to be linked to the FPGA unit: every time the function generator sends a TTL signal to the laser, it will simultaneously send a NIM signal to the FPGA, that will store it as a time-signal. However, the FPGA unit only handles LVDS signals in input, so, a signal converter is needed.

3.2.1 Checking signals synchronization

Teldyne LeCroy WaveRunner 9404M-MS oscilloscope has been used to test the actual synchronization of signals from the two output channels of the function generator. Hence, this latter device has been set to produce on both output terminals a pulse (square-wave) signal, with a 800 mV amplitude and a 10% duty cycle (Figure 3.8).
Then, the TTL output has been directly connected to the oscilloscope TTL input, that is terminated with a 50 Ω resistor. The NIM terminal has instead been connected to a Caen DT5495 programmable logic unit. The Caen unit works as a signal converter, transforming the NIM signal into a LVDS one. The LVDS signal has then been brought to the oscilloscope via cable to take proper synchronization measurements. The same LVDS signal will instead be sent to the FPGA in the final configuration for this set-

up. Figure 3.9 shows the oscilloscope and the Caen logic unit as arranged during signal synchronization analysis.

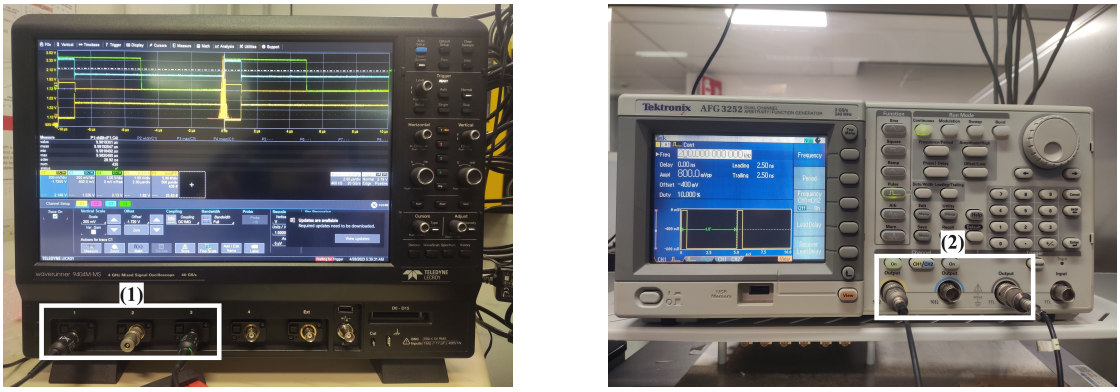

Figure 3.8: Close-up on the Teledyne LeCroy oscilloscope (left), equipped with a series of input terminals (1), including TTL and LVDS; close-up on Tektronix function generator (right), while setting parameters of the square-wave signals on the output channels (2).

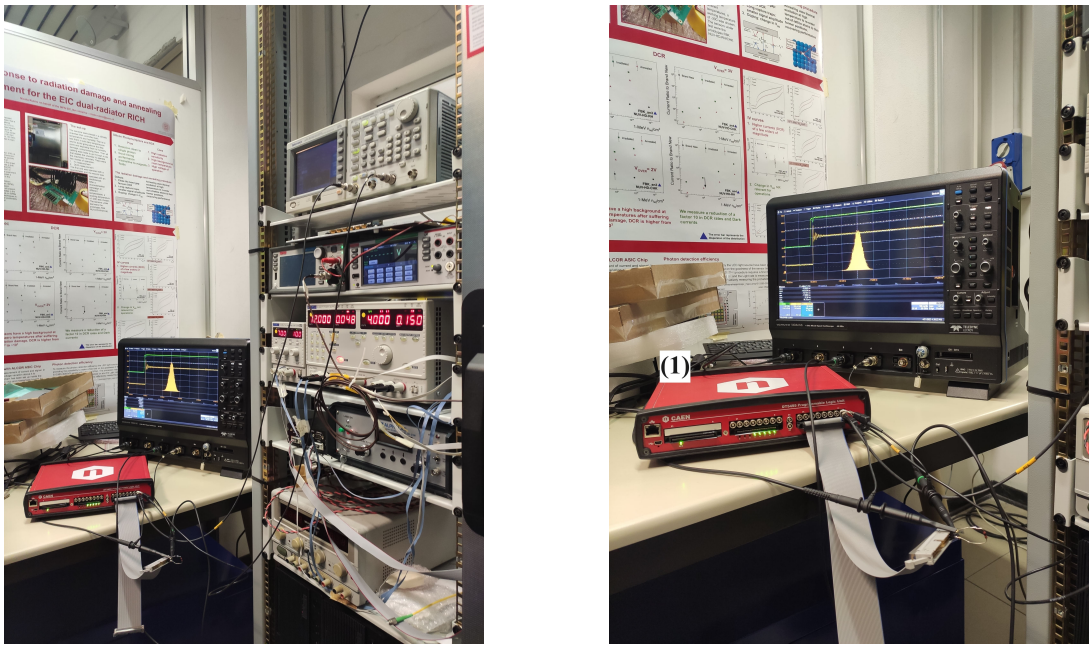

Figure 3.9: Overview on the arrangement for the analysis of NIM and TTL signals from function generator, via oscilloscope (left); close-up (right) on the oscilloscope and the Caen Programmable Logic Unit (1).

Both the TTL and the LVDS signals were displayed on the oscilloscope monitor, on a X-Y graph, showing wave amplitude (V) on the Y-axis and time (μs or ns) on the

X-axis. Synchronization between TTL and LVDS inputs has been verified by shifting one waveform at a time on the time-axis and checking if the other one would shift consequently on the same axis, by the same interval, in the same way. Waveforms shifting has been done through specific knobs integrated in the oscilloscope and it proved indeed that the two signals are synchronous.

3.2.2 Checking signals jitter

The output signals from the Tektronix function generator show small oscillations on the time-axis. This fenomenon is addressed with the term "jitter" and it affects the synchronization between NIM and TTL output signals. Therefore, it is relevant to quantify how these two signals oscillate in respect to each other; that means to measure the jitter between the NIM signal and TTL signal.
The Teledyne LeCroy oscilloscope is capable of measuring the relative time-variations of the two signals from the function generator. Furthermore, by taking repeated measurements of these variations, it is possible to populate a histogram on the oscilloscope display and extract a standard deviation, that is exactly the jitter value we want to measure (Figure 3.10). We can expect the histogram to be compatible with a gaussian distribution, as a single point in a wave signal undergoes random variations around a certain value on the X-axis.

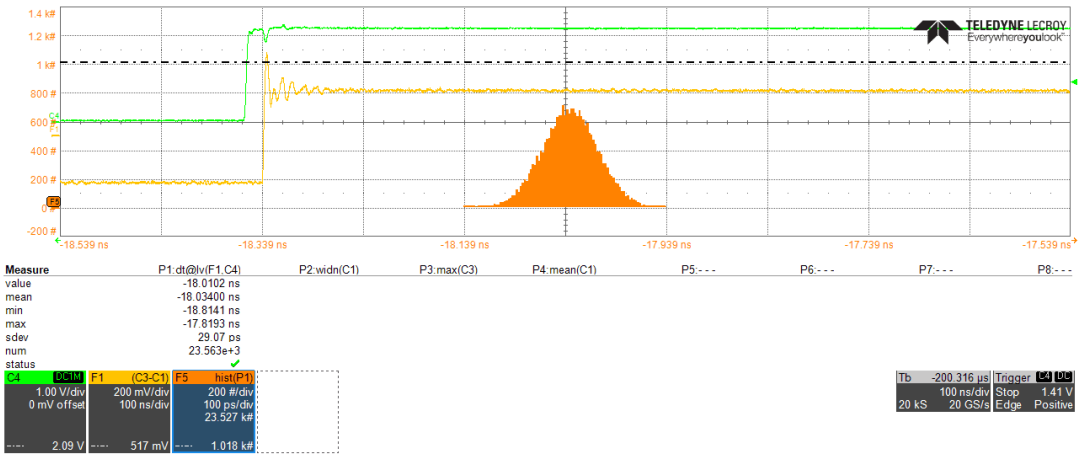

Figure 3.10: Screenshot of the scilloscope display, showing the LVDS signal from the Caen unit (yellow) and the TTL signal from the function generator (green); also, it shows the histogram (orange) populated with time-variations between the two signals; the histogram is compatible with a gaussian distribution and its RMS results 29 *ps*.

By keeping the same wave parameters on the function generator and by waiting the time necessary to get a significant population for the histogram, a jitter value of 29 *ps* has

been measured. We shall refer to this jitter value as j_1, for simplicity. Also, the histogram populated with time-variations between the two signals shows to be qualitatively compatible with a gaussian distribution.

The origin of the 29 ps jitter has been found by further analysis. This time, two TTL otuput terminals have been used from the pulse generator. These terminals are labelled as "Channel 1" and "Channel 2". The Tektronix device has been set to produce a square-wave of 1.65V amplitude and 10% duty cycle on both channels. Channel 1 has then been linked to the Teledyne LeCroy oscilloscope directly, while Channel 2 has been linked to the Caen unit. The Caen unit has been set to convert the TTL signal again into a LVDS output, that has then been sent to the oscilloscope.
By getting the difference between the two signals on the oscilloscpe and following the same steps as for the computation of j_1, the jitter between TTL and LVDS signals has been measured, getting a value of approximately 20 ps. We shall refer to this jitter value as j_2.
This last value must contribute to the j_1 value detected via oscilloscope. But j_2 is just about 2/3 of j_1, so there must be another contribute to it. As a matter of fact, there is actually an additional contribute that comes from the intrinsic jitter (j_{int}) of the pulse generator itself. By only connecting the function generator TTL output directly to the oscilloscope, j_{int} has been detected to lie in the $20 \div 25$ ps range. Jitter measurements are tidily collected in Table 3.1.

jitter value	measured value (ps)
j_1	29
j_2	20
j_{int}	$20 \div 25$

Table 3.1: Jitter values of the various signals analyzed using the Teledyne LeCroy oscilloscope; j_1 is the value of jitter between the TTL and NIM outputs of the function generator, j_2 is the jitter between the two TTL outputs of the generator and j_{int} the intrinsic jitter of the function generator.

As j_1, j_2 and j_{int} are standard deviation values, it is then possible to use error propagation properties to check if it is true that j_2 and j_{int} solely contribute to j_1. Specifically, this can be verified by computing j_1 as the square-sum between j_2 and j_{int} and comparing it to the measured value for j_1:

$$j_1 = \sqrt{(j_2)^2 + (j_{int})^2} \approx \sqrt{(20\ ps)^2 + (22.5\ ps)^2} \approx 30\ ps; \tag{3.4}$$

where 22.5 ps is the mean value in the $20 \div 25$ ps range for j_{int}.

Calculation 3.4 confirms that the total jitter between the TTL signal and the NIM signal generated by the function generator (j_1) is due to a combination of the intrinsic jitter (j_{int}) of the function generator itself and the jitter between two TTL signals also generated by the function generator (j_2).

Jitter may be reduced by actioning the laser directly, without any intermediate device. Again, however, the diode laser used in this set-up does not allow for remote control and therefore the preference has been to keep the setup with an externally-pulser-driven laser.

3.3 Laser characterization

Once signals from the Tektronix function generator have been analyzed, the final configuration to characterize the ALPHALAS diode laser has been arranged.
The function generator NIM output is linked to the Caen unit, that converts the signal into a LVDS one and sends it to the FPGA unit. Also, the TTL terminal on the function generator is direclty connected to the diode laser. This way, by setting an output square-wave from the Tektronix device, each time the wave-form rises at its maximum (i.e. a maximum voltage) it turns the laser on and then turns it off when reaching a minimum. This means the laser needs to work in pulser mode and its pulser frequency will correspond to the signal frequency from the function generator. At the same time, when the signal reaches its maximum, the FPGA stores it as a time-signal, corresponding to the laser activation.

The idea is to utilize the laser to light up the SiPM sensors in the climatic chamber and use data from the sensors to characterize the laser itself. This process requires data from SiPMs to be reliable, that means that efficiency on photon detection via SiPMs has to be constant and consistent. Luckly, on the proper SiPMs used in this apparatus, a series of tests have been previously conducted, showing that the sensors do keep consistent performance when kept at low temperature inside the MEMMERT chamber [11].
At this point, it has been necessary to verify:

- if the fibers and filters set-up allows for enough or any light to reach the SiPM sensors;
- if the laser TTL input needs to be terminated with a resistor in order to communicate properly with the function generator;
- if the SiPM sensors can actually detect one photon at a time, that is, if the probability for the sensors to detect more than one photon is negligible compared to the probability of detecting one single photon.

The above three points are adressed in the following paragraphs.

3.3.1 Checking laser light intensity

The whole optical filters and fibers set-up, as described in Section 3.1, may just reduce the light beam intensity up to a point where it would not be able to trigger the sensors and therefore not allowing to distinguish a light pulse signal from noise signals.

First, in order to verify if the filters arrangement actually allows for some laser light to reach the end of the fiber path, a visual test has been conducted.
As the fiber cable terminates into a collimator fixed on a mount inside the climatic chamber, the door of this latter has been set open, in order to be able to see laser light exiting the collimator. Then, the ALPHALAS laser has been set in continuous-wave mode. A pair of Global Laser safety glasses (Figure 3.11) have been used in order to avoid potential eye damage from laser light. Also, room lights have been switched off in order to be able to discern the light beam more easily.

Figure 3.11: Global Laser safety glasses; this model blocks light within the wavelength range of $\sim$840$\div$1090 nm.

Then, by acting directly on the bespoken laser knob, labelled as "continuous wave power", the light beam power has been increased up to a point where it is visible through the safety glasses. Eventually, it has been possible to distinguish a luminous semi-violet dot being projected on a white paper at maximum pulse power.
This test gives a first rough, but significant, proof that laser light is able to pass through the optical filters series and reach the end of the optical fiber pathway and therefore reach the SiPM sensors inside the climatic chamber.

Using a custom PC programme, the X-Y movement system on which the SiPMs are mounted has been moved so that the light spot would just cover the one HAMAMTSU

S13360-3050VS sensor (Figure 3.12). We may refer to this sensor as A1, following its naming in the custom program used for data analysis.

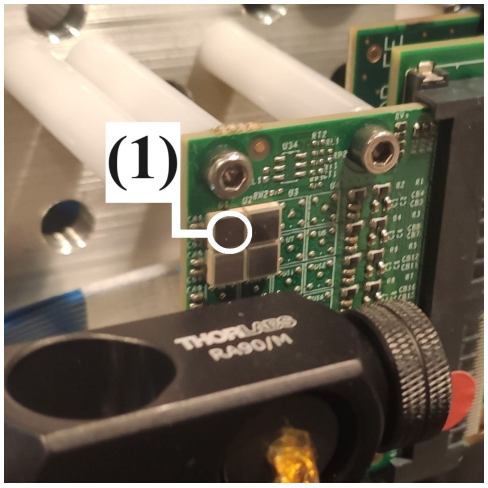

Figure 3.12: Close-up on the SiPM sensors used in the set-up, including the HAMAMATSU S13360-3050VS sensor (1).

3.3.2 Noise at room temperature

As mentioned in Section 3.2, when connecting the TTL output of the function generator to the TTL input of the oscilloscope, it is key that this latter terminal is terminated with a 50 Ω resistor, so that signal interchange works properly. Data sheet relative to the ALPHALAS laser doesn't specify weather the device's TTL input terminal is terminated with a 50 Ω resistor or not.
In order to know if an external resistor is needed, it has been necessary to test the SiPMs response to the laser light. The assumption that has been followed is simple: by using both the function generator and the laser in pulser mode, as SiPMs reliability on photon detection is not at doubt, it would be expected for their photon detection rate to increase linearly with the increase of the pulser frequency; if this is the case, it would mean that the laser pulser frequency itself corresponds to the function generator frequency and therefore there would be no need for an external resistor. Also, both the Tektronix function generator and the ALPHALAS diode laser come with a display that show the device's pulser frequency, so it is possible to check if frequencies coincide from there.

The effectiveness of the wiring between pulser generator and laser has been verified alongside the tests on the detection rate of reference A1 SiPM.

SiPM sensors are powered by the high voltage (HV) supply. As explained in Section 2.2, voltage applied to the SiPMs must be high enough to overcome the sensors' breakdown voltage (Table 3.2). This way, it will be possible to observe a peak signal when sensors are lit by the laser light.

Temperature (°C)	Breakdown Voltage (V)
25	~ 51
-30	~ 48

Table 3.2: Breakdown voltage values of the reference A1 SiPM used in this set-up; 25 °C and -30 °C are considered to be respectively room temperature and minimum temperature inside the climatic chamber.

Once HV is turned on, the sensors will inevitably detect noise from it, as well as from surrounding electronics. Detected noise translates into a voltage signal that is not relevant to the proper measurements relative to the sensors' light response. Therefore, noise signals shall be neglected. In order to do that, it is needed to find the maximum voltage value reached by noise signals, that is the threshold voltage above which noise is not counted.
Consequently, a custom software has run to perform a discrete sweep in voltage threshold, from a minimum bias voltage to a maximum. Each actual threshold value is associated to an integer, positive number from 0 to 63, that will be shown on PC terminal next to the correspondent detection rate from the sensors. This first threshold scan has been operated at room temperature.
This scan has shown that noise rate from the reference A1 sensor reaches a top 230 kHz and rate is zero for threshold values above 10. Hence, in order for electronics to neglect this noise signal, threshold has been set to number 11 in the bespoken PC programme.

3.3.3 Detection rate and probability

A key feature is for the reference A1 sensor to detect no more than one photon at a time. It is then necessary to minimize the probability of two or more photons reaching the sensor.
The probability of detecting n photons is described by the Poisson distribution:

$$P(n;\lambda) = \frac{\lambda^n}{n!} \cdot e^{-\lambda} \qquad \forall n \in N; \tag{3.5}$$

where λ is the mean value of the distribution. We want $\lambda = 0.01$ in order for the probability of revealing more than one photon to be negligible compared to the probability of revealing one photon. In fact, by using $\lambda = 0.01$ in Equation 3.5, we find:

$P(1; 0.01) \sim 9.9 \cdot 10^{-3}$ and $P(2; 0.01) \sim 5.0 \cdot 10^{-5}$.
From here, it follows that $P(2; 0.01)/P(1; 0.01) \sim 5.0 \cdot 10^{-3}$ and we can therefore assume that $P(n > 1; 0.01)$ is neglibile.

In practice, the mean value λ of the Poisson distribution corresponds to the mean probability of detecting a signal from the SiPM sensor consequently to a laser pulse. This last observation implies that if we want $\lambda = 0.01$, we then have to make sure that the whole optical system (laser, optical fibers, ND filters, light collimator) works in a way that, for each laser pulse, the mean number of photons reaching the SiPM sensor would be 0.01. In other words, we want the photon detection rate from the reference SiPM to be as close as possible to 1% of the laser's pulse rate.
This outcome also depends on the SiPM's photon detection efficiency. Photon detection efficiency of the reference A1 sensor depends on the wavelenght of incident light (Section 2.2, Figure 2.6) and the ALPHALAS laser emits light at a declared constant wavelenght of 401.4 nm, to which corresponds a 38% efficiency for the A1 sensor at room temperature.

In order to test the proper functioning of the set-up as described so far, a frequency scan on the reference SiPM has been operated.

3.3.4 Frequency scan

The MEMMERT chamber's door has been closed, for a cooling cycle to be then initiated, from room temperature to -30 °C. So, the high voltage supply has been set to 51 V. The Tektronix function generator has been set to send a pulsed signal to the laser, varying pulser frequency in a preset discrete range. Hence, the ALPHALAS laser has been set in pulser mode. For each frequency value, detection rate from the reference SiPM sensor has been recorded.

Figure 3.13 and Figure 3.14 show distributions of 100 samples of photon detection rate. The shape of these distributions is in accordance with expectations: SiPMs' photon detection is affected by a random error, that produces a Gaussian distribution of counts rate around a mean value. Graphs have been produce using the ROOT framework and as we can see from them, Gaussian forms are higly piked on their mean value.

In specific, graph in Figure 3.13 shows noise detected by the A1 sensor at -30 °C.

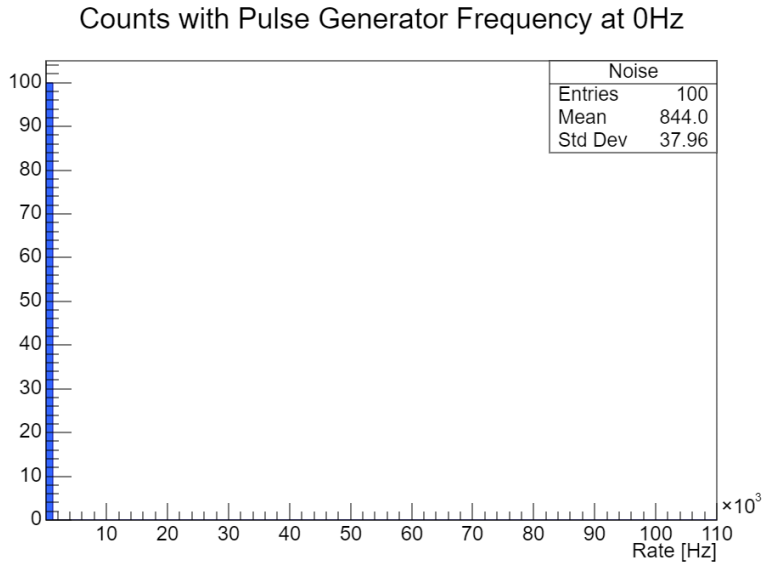

Figure 3.13: Distribution of 100 samples of photon count rate from the reference A1 SiPM, when not lit by the laser light.

Taking into account noise counts for graphs in Figure 3.14, it is noticeable that each distributions' mean value is close to the function generator frequency divided by 100. In other words, for each graph, the A1 SiPM's rate increases above noise by the same frequency of the function generator, divided by a factor of 100. This means that the whole optical system works correctly, providing that for a certain number of photons generated by the laser, just 1% of it actually reach the SiPM. It also implies that the laser successfully produces a pulsed light-signal that has the same frequency set from the pulser generator.

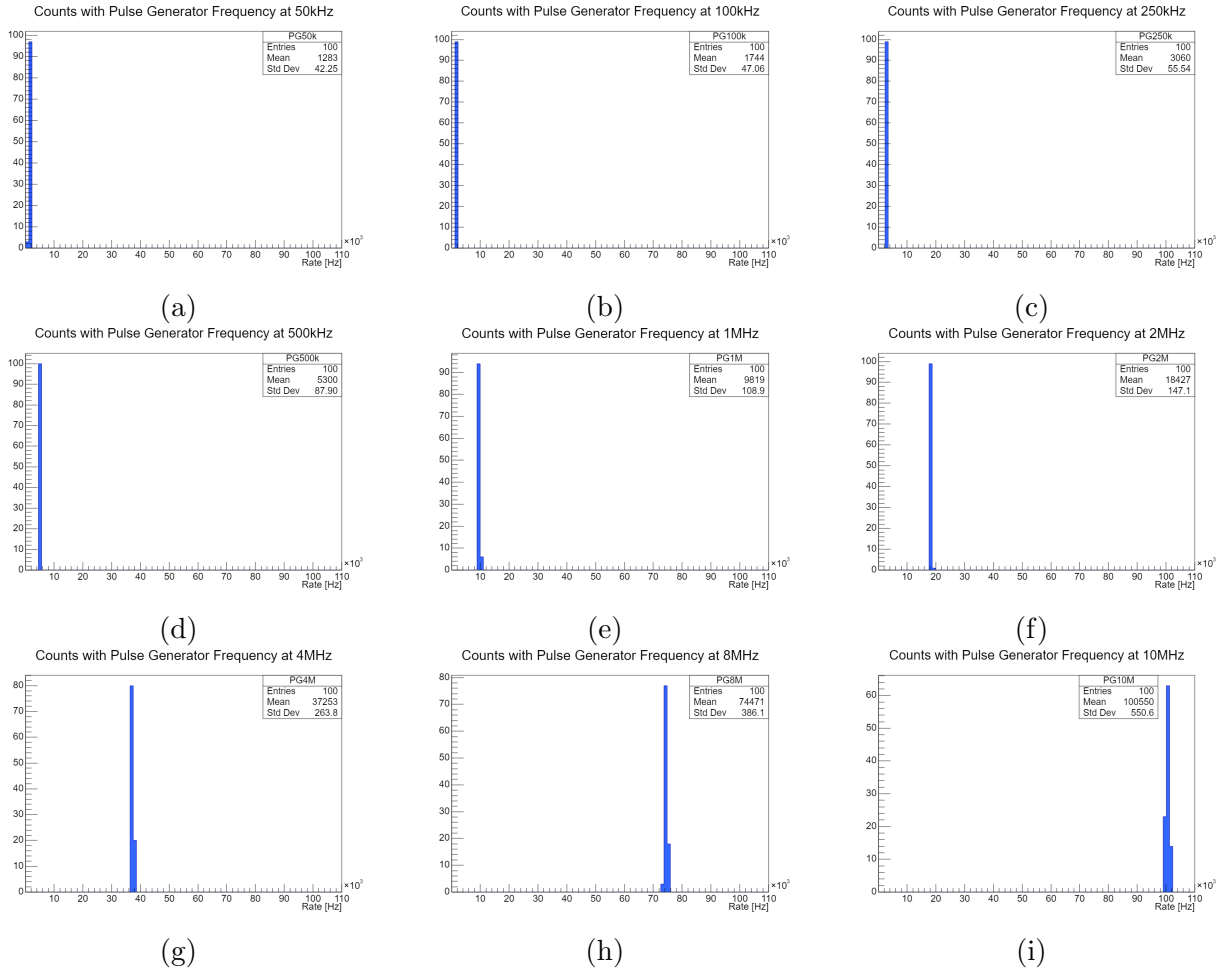

Figure 3.14: Distribution of 100 samples of photon count rate from the A1 sensor, when lit by the laser light at a fixed pulser frequency.

One relevant quantity to calculate is the ratio between mean photon detection rate and pulser frequency, for each of the above distributions. It is evident that by computing this ratio we are just computing the probability of detecting at least one photon. Graphs in Figure 3.14 report mean detection rate values, from which we can compute probability and represent it as a function of pulser frequency, as in Figure 3.15.

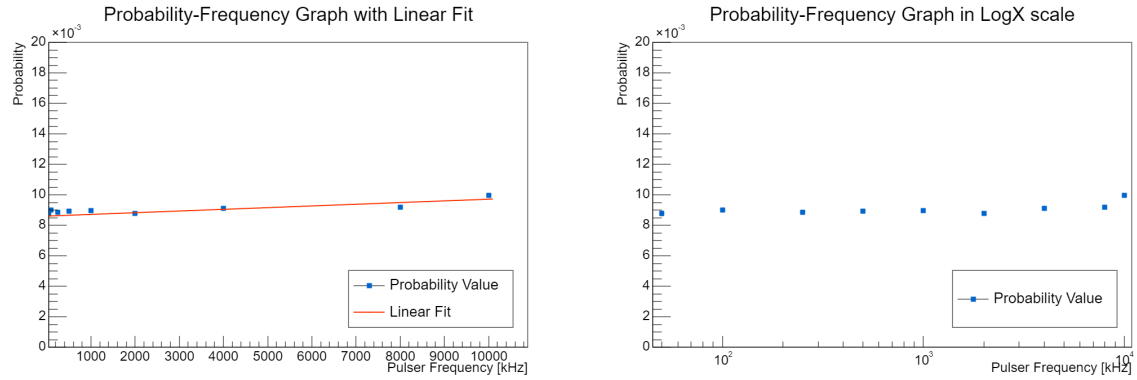

Figure 3.15: Photon detection probability as a function of pulser generator frequency; straight line fitted to data (left) highlights probability trend on pulse frequency; X-axis set in logarithmic scale (right) to better visualize markers at lower pulser frequencies.

Fit parameters from Figure 3.15 have been computed by the ROOT framework and their values are reported in Table 3.3.

Fit parameters	
$p0$	$p1$
$(8.60 \pm 0.01)\cdot 10^{-3}$	$(1.11 \pm 0.01)\cdot 10^{-7}$

Table 3.3: Linear fit (Figure 3.15) parameters computed by the ROOT framework; $p0$ is the origin ordinate of the straight line and $p1$ its angular coefficient.

From Figure 3.15, it is then possible to extrapolate one key information. In fact, probability values at each pulser frequency range from $8.8\cdot 10^{-3}$ (at 50 kHz pulser frequency) to $9.9\cdot 10^{-3}$ (at 10 MHz pulser frequency) and this means that we have a mean detection probability that is well approximable to 1%. This is consistent with the above analysis on detection rates for graphs in Figure 3.14.
However, from fit parameters in Table 3.3, we note that the fit function cannot be considered as parallel to the X-axis and therefore the probability cannot be considered as constant over the chosen function generator frequencies interval. In specific, it is noticeable how the fit trend on detection probability suggests that this latter should increase as a function pulser frequency increases. This last aspect is inspected in the following paragraph.

3.3.5 Detection rate and laser power

Mean detection rates from graphs in Figure 3.14 are then linearly proportional to the function generator frequency. This linear relation is well noticeable in Figure 3.13.

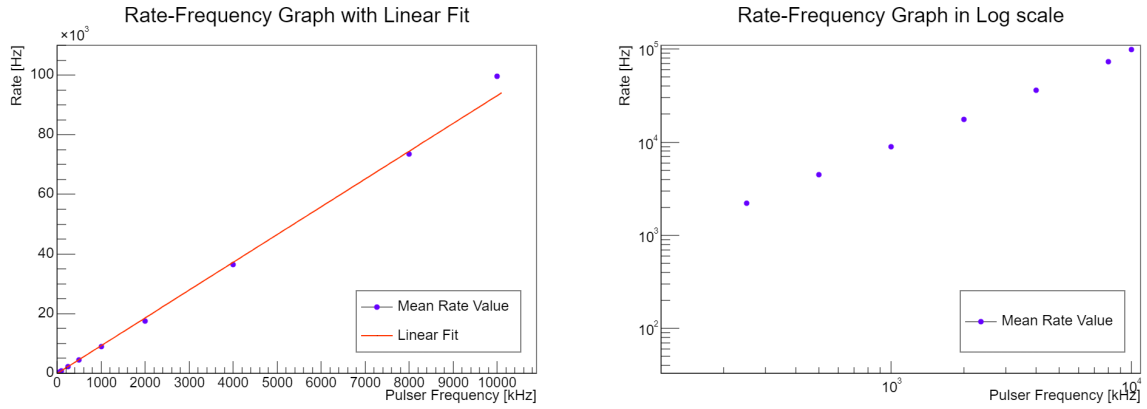

Figure 3.16: Mean photon count rate as a function of pulser frequency; straight line fitted to data in range between 0 Hz and 10 MHz (left); graph in logarithmic scale on both axes (right) better shows rate values at low pulser frequencies.

However, also from Figure 3.16 (left), we can see how the one marker indicating the rate of detected photons at 10 MHz pulser frequency is shifted from the fit function profile, as if there was no linear relation between this rate and the others.
This is no fortuity: even repeating detection at 10 MHz, linear function doesn't quite fit data. We can quantify discrepancy between expected rate (R_E) from the linear fit and measured mean rate values (R_M) from the reference SiPM, by calculating the so called residues ($resid$):

$$resid = |R_M - R_E|/R_M = |R_M - (p0 + p1 \cdot f)|/R_M; \tag{3.6}$$

where f is the pulser frequency, $p0$ and $p1$ are respectively the origin ordinate and angular coefficient of the fit straight line. $p0$ and $p1$ have been computed by the ROOT software and their values are reported in Table 3.4.

Fit parameters	
$p0$ (Hz)	$p1$
-73.0 ± 21.9	9.32 ± 0.03

Table 3.4: Linear fit (Figure 3.16) parameters computed by the ROOT framework; $p0$ is the origin ordinate of the straight line and $p1$ its angular coefficient.

Figure 3.17 shows residues as a function of pulser frequency, in logarithmic scale. It is evident how for some frequency values, residues' values are higher: in specific, at 50

kHz and 10 MHz pulser frequency we have the highest residues, about 10 times higher compared to the residue at 8 MHz, according to the y-axis scale.

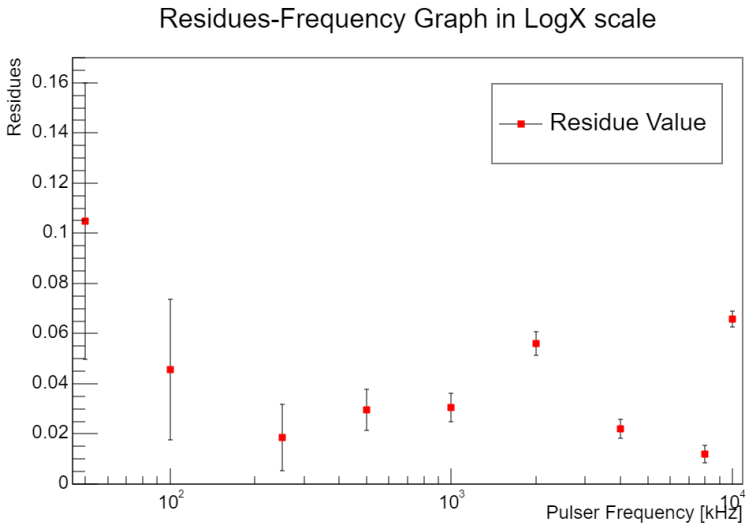

Figure 3.17: Graph showing residues (Equation 3.6) as a function of the generator frequency; X-axis set in logarithmic scale, for an easier identification of markers.

A possible cause for the discrepancy between expected and detected rate at 10 MHz can be related to the laser. This inconvenience is relevant, as the reliability of the whole set-up depends on its resolution, or at least on the identification of its origin.

One important aspect to check has been the laser pulse power. In fact, as described in Section 3.1, the rate of detected photons from the A1 sensor depends on the intensity of impacting light beam. And luminous intensity is directly proportional to the beam power (Equation 3.2).
The ALPHALAS laser data sheet provides average power measurements at different frequencies, when device is set in pulser mode (Table 3.5).

Frequency (Hz)	Pulse Width (ps)	Average Power (μW)
100	23.9	0.005
1k	24.9	0.051
10k	24.3	0.568
100k	24.7	5.85
1M	24.7	60
5M	24.7	312
10M	24.3	670
15M	24.7	965
20M	24.1	1350

Table 3.5: Laser light average power measurements, taken at different frequency values, when laser is set in pulser mode; also, time-width of pulses is provided for each frequency value; measurements provided by the device's specific data sheet; errors not specified.

Figure 3.18 (left) shows linear relation between average laser power and pulser frequency.

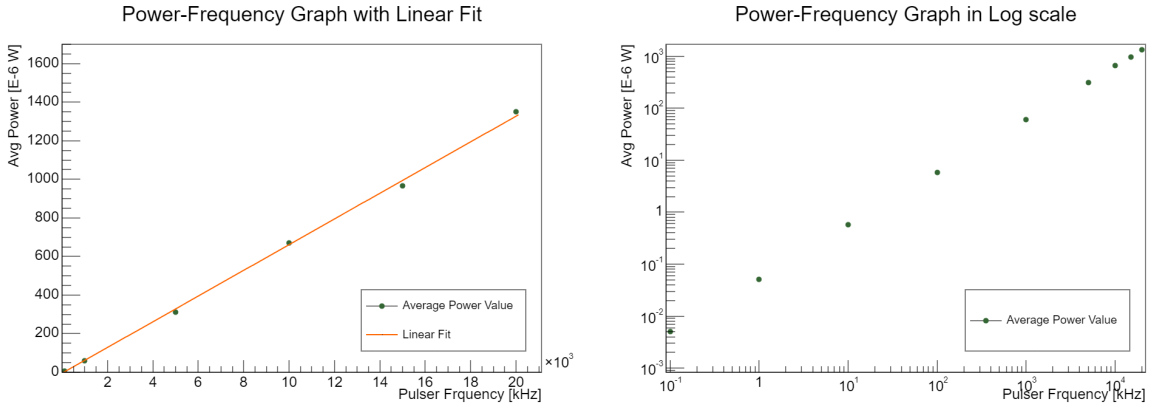

Figure 3.18: Laser average power as a function of pulser frequency; fit with a straight line in the range between 100 Hz and 20 MHz (left); graph in logarithmic scale on both axes (right) better shows rate values at low pulser frequencies; data from Table 3.5.

Also for fit in Figure 3.18, the $p0$ and $p1$ parameters are given by ROOT, and their values are reported in Table 3.6.

Fit parameters	
$p0$ (μW)	$p1$
-4.61 ± 6.82	(666.18 ± 7.47)·10^{-4}

Table 3.6: Linear fit (Figure 3.18) parameters computed by the ROOT framework; $p0$ is the origin ordinate of the straight line and $p1$ its angular coefficient.

Then, detection rate from the reference A1 sensor has been measured for a new set of pulser frequencies: 1 kHz, 10 kHz, 100 kHz, 1 MHz, 5 MHz and 10 MHz. This in order to get count rates at the same frequencies at which average laser power measurements have been taken. By computing the ratio between count rate and laser power, we'd expect to find results close to each other for each value of pulser frequency.

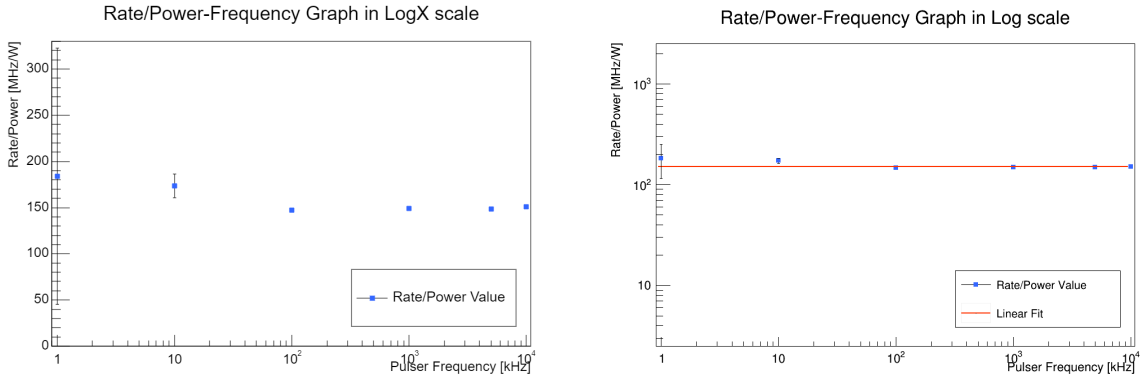

Figure 3.19: Graphs showing ratio between count rate from SiPM and average laser pulse power, as a function of pulser generator frequency; logarithmic scale on X-axis allows better markers visualization (left); both axes are set in logarithmic scale for a proper visualization of the linear fit in range between 1 kHz and 10 MHz (right).

Fit parameters	
$p0$ (MHz/W)	$p1$
147.41 ± 0.16	(3.23 ± 0.20)·10^{-4}

Table 3.7: Linear fit (Figure 3.19) parameters computed by the ROOT framework; $p0$ is the origin ordinate of the straight line and $p1$ its angular coefficient.

Figure 3.19 shows that detection rate from SiPMs on laser average power at 100 kHz, 1 MHz, 5 MHz and 10 MHz pulser frequencies is almost constant, at least from a qualitative point of view. The straight line doesn't quite fit data at 1 kHz and 10 kHz frequency, however, this effect may be due to background noise imprecisions, even if noise count rate is subtracted (as it is in this case).

Anyway, fit parameters from ROOT calculations (Table 3.7) do show a trend: the ratio between detection rate and average laser power from data sheet slightly increases with pulse frequency in the range between 100 kHz and 10 MHz.
This latter result, toghether with graph in Figure 3.18 (left), suggests that the average laser pulse power increases non-linearly with respect to the laser pulse frequency.

3.3.6 Threshold scan

Once the laser has been characterized, a series of tests has been conducted on the reference SiPM to probe its response to the laser light.
Again, the photon detection rate from the A1 sensor has been recorded, but this time a threshold scan has been performed, instead of a frequency scan. Also this new test has been conducted at -30 °C inside the climatic chamber. By keeping a fixed pulser frequency, 25 samples of count rate have been collected at different voltage threshold values. As explained in previous paragraphs, threshold is changed through a bespoken software, that associates actual voltage values to an integer set of numbers, from 0 to 63.

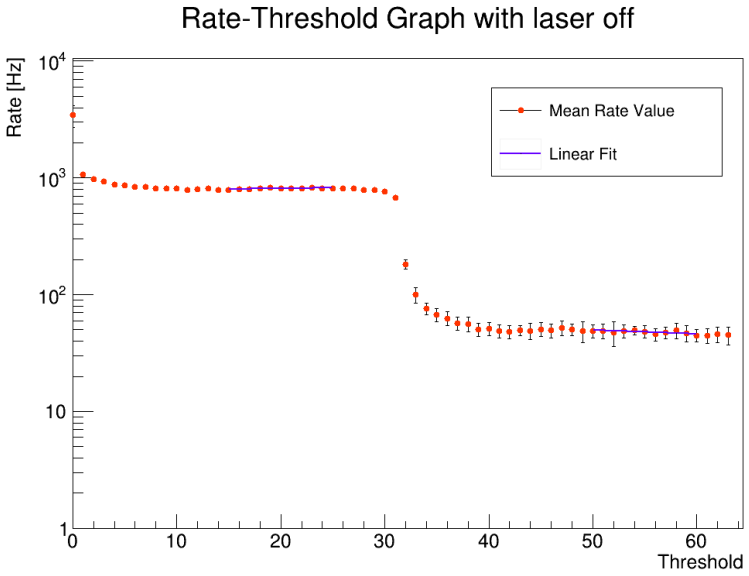

Figure 3.20: Distribution of mean measurements of photon detection rate from the reference A1 SiPM, as a function of the threshold voltage at which data acquisition is triggered; pulser generator is off and so the laser doesn't emit any light; a straight line is fitted in two ranges of the X-axis: 15÷25 and 50÷60.

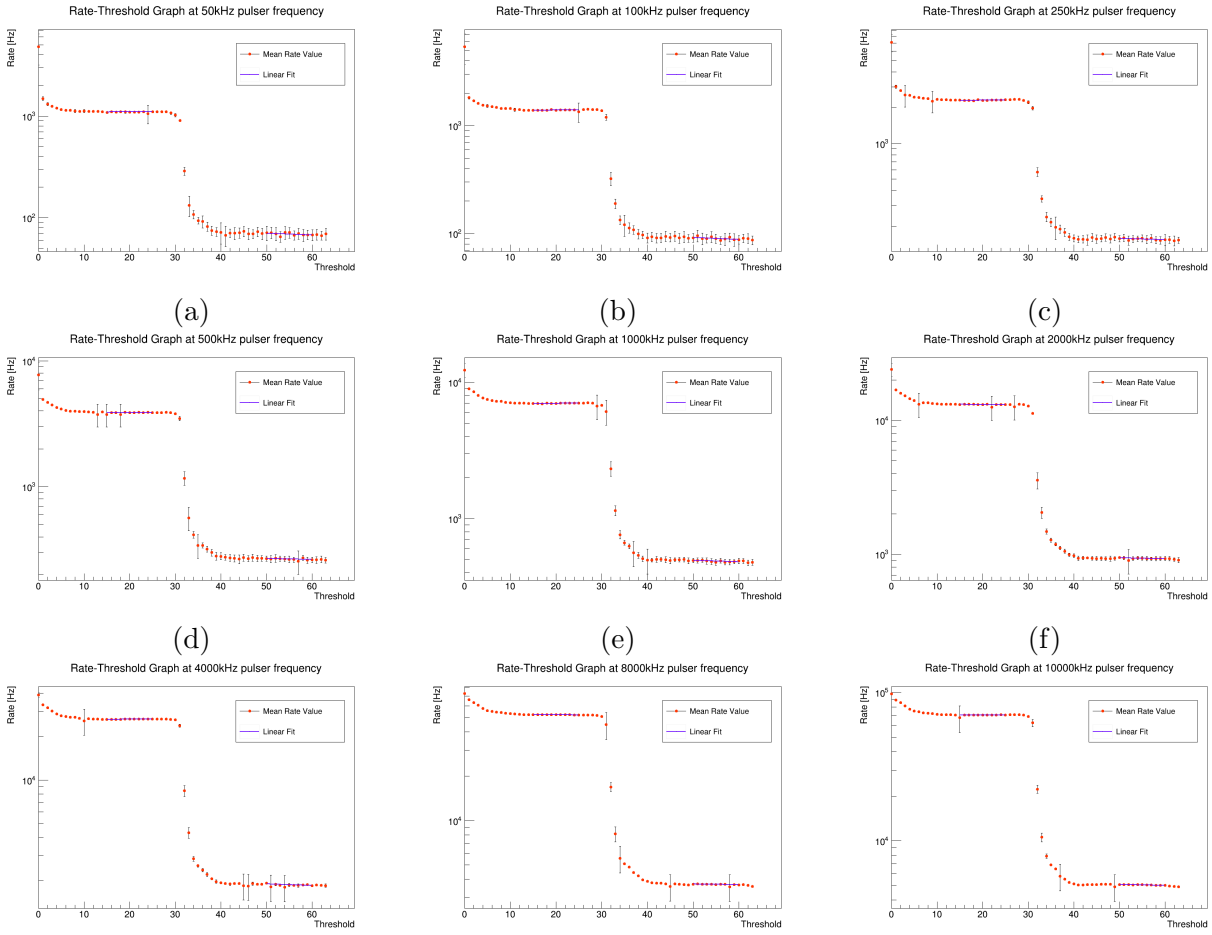

Figure 3.21: Distributions of mean measurements of photon detection rate from the reference A1 SiPM, as a function of the threshold voltage at which data acquisition is triggered, with laser on at different pulser frequencies; a straight line is fitted in two ranges of the X-axis: 15÷25 and 50÷60.

From Figure 3.20, two plateaus are noticeable: a first one at a higher rate and a second one at a lower rate. Also, we notice a first step near zero threshold value and a second between the plateaus.
Mean SiPM count rate from first plateau corresponds to the rate compatible with revealing at least one photon.
Mean SiPM count rate from second plateau corresponds to the rate compatible with revealing more than one photon, i.e. at least two photons.
As Figure 3.20 shows, a stright line is fitted to data in two arbitrary ranges, that are distant enough from the steps. Fit parameters computed by the ROOT framework are:

- in range 15÷25, $p0$ = (827.8 ± 51.3) Hz and $p1$ = -3.10 ± 2.54;
- in range 50÷60, $p0$ = (43.9 ± 39.9) Hz and $p1$ = 0.04 ± 0.72;

where $p0$ is the origin ordinate of the straight line and $p1$ its angular coefficient.

Also for graphs in Figure 3.21, a straight line is fitted to data on each plateau in a small arbitrary range, distant enough from the steps. Table 3.8 reports fit parameters calculated by the ROOT framework; these parameters are useful for deeper analyses.

Pulser Frequency (Hz)	Range 15÷25	Range 50÷60
50k	$p0$ = (1357.3 ± 65.2) Hz $p1$ = -2.97 ± 3.13	$p0$ = (82.7 ± 45.9) Hz $p1$ = 0.03 ± 0.84
100k	$p0$ = (1781.1 ± 75.2) Hz $p1$ = 2.41 ± 3.79	$p0$ = (130.2 ± 58.4) Hz $p1$ = -0.15 ± 1.06
250k	$p0$ = (3487.1 ± 109.8) Hz $p1$ = -2.45 ± 5.50	$p0$ = (267.1 ± 81.3) Hz $p1$ = -0.56 ± 1.49
500k	$p0$ = (6148 ± 127) Hz $p1$ = -0.21 ± 6.34	$p0$ = (507 ± 110) Hz $p1$ = -1.60 ± 2.00
1M	$p0$ = (11504 ± 228) Hz $p1$ = -0.8 ± 10.8	$p0$ = (876 ± 144) Hz $p1$ = -1.30 ± 2.60
2M	$p0$ = (21651 ± 304) Hz $p1$ = 2.53 ± 15.1	$p0$ = (1750 ± 197) Hz $p1$ = -4.23 ± 3.62
4M	$p0$ = (42959 ± 351) Hz $p1$ = -13.5 ± 17.3	$p0$ = (3207 ± 289) Hz $p1$ = -4.01 ± 5.24
8M	$p0$ = (84229 ± 509) Hz $p1$ = 54.3 ± 25.1	$p0$ = (7198 ± 399) Hz $p1$ = -19.75 ± 7.25
10M	$p0$ = (116433 ± 697) Hz $p1$ = 2.86 ± 35.48	$p0$ = (9606 ± 528) Hz $p1$ = -26.32 ± 9.50

Table 3.8: Linear fit (Figure 3.20 and Figure 3.21) parameters computed by the ROOT framework; $p0$ is the origin ordinate of the straight line and $p1$ its angular coefficient.

It is noticeable that for each fit uncertainty on the angular coefficient $p1$ is large enough, compared to $p1$ itself, to consider the straight lines to be all parallel to the X-axis. Therefore, we can assume that the origin ordinate $p0$ well approximates the mean rate value in the fit range.
Therefore, from fits to the highest plateau at each pulser frequency, we get a set of $p0$ mean rates of detections of at least one photon from the reference sensor, that correspond to the rates measured during frequency scan tests, reported in previous paragraphs.
Hence, by representing $p0$ values as a function of pulser frequency, we expect to obtain a graph that is qualitatively comparable to the one in Figure 3.16.

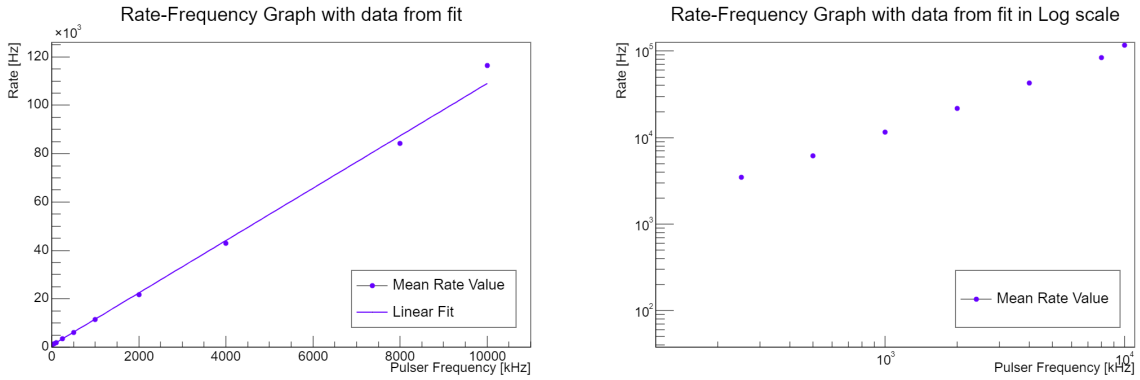

Figure 3.22: Mean photon count rate as a function of pulser frequency; straight line fitted to data in range between 0 Hz and 10 MHz (left); graph in logarithmic scale on both axes (right) better shows rate values at low pulser frequencies.

Figure 3.22 shows $p0$ values as a function of pulser frequency. Table 3.9 reports parameters relative to the straight line fitted to graph in Figure 3.22 (left).

Fit parameters	
$p0$ (Hz)	$p1$
690.7 ± 30.7	6.58 ± 0.03

Table 3.9: Linear fit (Figure 3.22) parameters computed by the ROOT framework; $p0$ is the origin ordinate of the straight line and $p1$ its angular coefficient.

Actually, the origin ordinate $p0$ in Table 3.9 takes noise into account. And count rate due to noise is (827.8 ± 51.3) Hz as reported above. We shall then compute:

$$p0' = p0 - noise = [(690.7 - 827.8) \pm (30.7 + 51.3)]\ Hz = (-137.1 \pm 82.0)\ Hz; \quad (3.7)$$

where linear error propagation is used. This latter result has been double checked with the ROOT framework.

We now name $p1$ from Table 3.9 as $p1'$. Also, let's recall fit parameters $p0$ and $p1$ from Table 3.4, relative to the fit function in Figure 3.16 (left) and name them $p0_m$ and $p1_m$ respectively, not to get confused. This way, we can compare:

- $p0'$ = (-137.1 ± 82.0) Hz and $p0_m$ = (-73.0 ± 21.9) Hz;
- $p1'$ = 6.58 ± 0.03 and $p1_m$ = 9.32 ± 0.03.

It's noticeable that $p0_m$ and $p0'$ are compatible within the error. For what concearns $p1_m$ and $p1'$, even though they are not compatible within the error, they're still of the same order of magnitude, so that we can consider the graphs in Figure 3.22 compatible with the ones in Figure 3.16, at least from a qualitative point of view.

Crosstalk (Paragraph 2.2.3) in a SiPM is responsible for the generation of a signal with similar characteristics (i.e. charge and amplitude) of signals from the detection of multiple photons in a given laser pulse. The crosstalk rate can be evaluated as mean detection rate from the second plateau with no impinging light, since in that case multiple events can only be triggered by crosstalk between cells. Crosstalk probability can then be evaluated as the ratio between mean detection rate from the second and the first plateau. Fit parameters show that the fit straight line in Figure 3.20 is consistent with a constant trend. Therefore the fit has been repeated with a constant function and the crosstalk probability consequently calculated results $P_C = (5.60 \pm 0.59) \cdot 10^{-2}$.

Further, we can compute the probability of events triggered by more than one delivered photon as the difference between the crosstalk rate and mean detection rate from the second plateau, normalized to the pulser frequency. We expect this probability to be constant as a function of the pulser frequency, as Figure 3.23 shows.

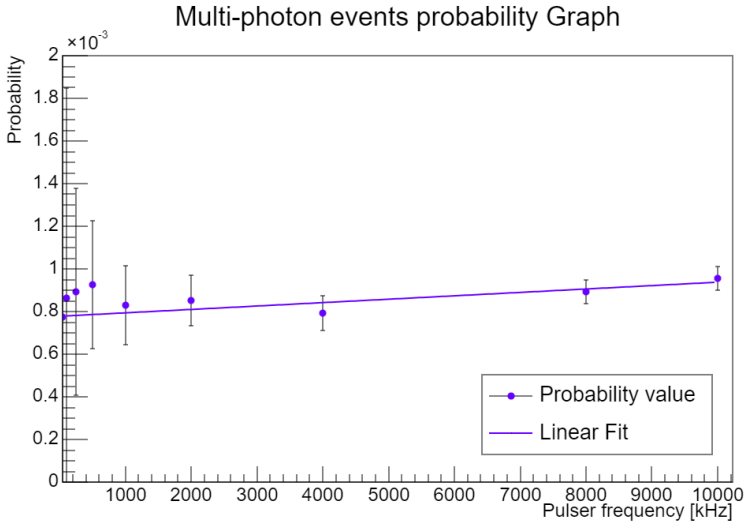

Figure 3.23: Measured probability of multi-photon events as a function of pulser frequency; straight line fitted to data.

Given the large error on the angular coefficient $p1$ from Table 3.10, the fit straight line in Figure 3.23 is consistent with a constant trend. For this reason the fit has been repeated with a constant function to obtain the probability of events triggered by more than one delivered photon, that is $P_M = (8.94 \pm 0.33) \cdot 10^{-4}$, which is negligible compared to the

crosstalk probability P_C. This confirms that the contamination from events with more than one delivered photon from the laser system is negligible and the set-up allows for SiPM characterization in the single-photon regime.

Fit parameters	
$p0$	$p1$ (kHz^{-1})
$(7.79 \pm 0.87)10^{-4}$	$(1.60 \pm 1.11)10^{-8}$

Table 3.10: Linear fit (Figure 3.23) parameters computed by the ROOT framework; $p0$ is the origin ordinate of the straight line and $p1$ its angular coefficient.

3.3.7 Changing the light collimator

At last, the light collimator at the end of the optical fiber path has been replaced with another one, that produces a larger illumination area.
The two collimators are structurally different, so, in order to keep the new one in place, the mount support inside the climatic chamber has been also changed (Figure 3.24).

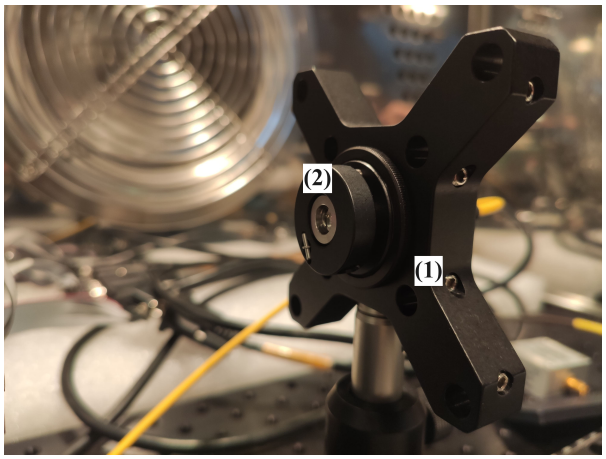

Figure 3.24: Close-up on the sight (1) used to support the last mounted collimator (2) inside the climatic chamber.

Because of the new sight, the collimator's distance from the SiPM sensors has been adjusted, as well as the position of the board supporting the sensors.
Once all set, the diameter of the new circular illumination area has been measured using a graph paper, getting a value of $\emptyset \approx 1$ mm.

With this new set-up, a new threshold scan at -30 °C has been performed, in orderd to

test again its correct functioning from the A1 reference SiPM.

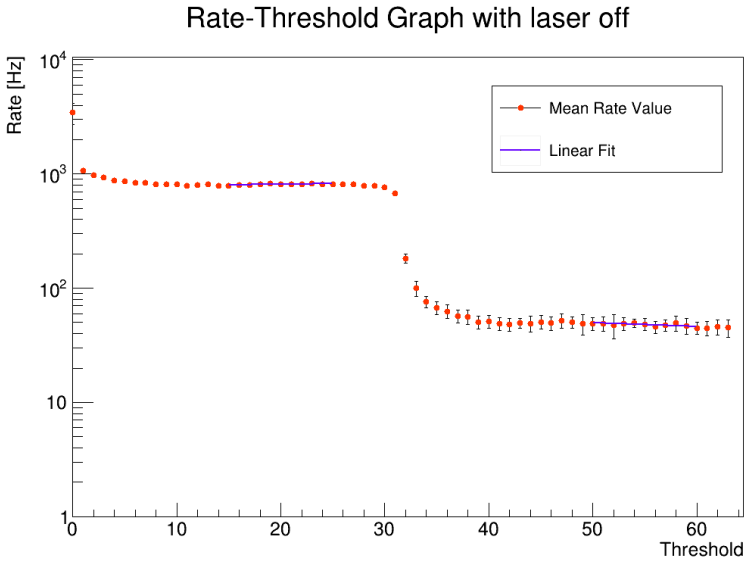

Figure 3.25: Distribution of mean measurements of photon detection rate from the reference A1 SiPM, as a function of the threshold voltage at which data acquisition is triggered; pulser generator is off and so the laser doesn't emit any light; a straight line is fitted in two ranges of the X-axis: 15÷25 and 50÷60.

Figure 3.25 and Figure 3.26 show the distributions of mean detection rate from the A1 SiPM, as a function of threshold voltage. Graphs are analogous to the ones from Figure 3.20 and Figure 3.21.

Graphs in Figure 3.25 and Figure 3.26 show the same plateaus seen previously in Figure 3.20 and Figure 3.21. Again, for each plateau, a straight line is fitted to data on a small arbitrary range, distant enough from the steps for the distribution profile to be considered parallel to X-axis in that range. Obviously, fit parameters will differ for this new threshold scan, but the new curve shapes are compatible with the ones from the previous scan, confirming the correct functioning of the final arrangement with a different light collimator.

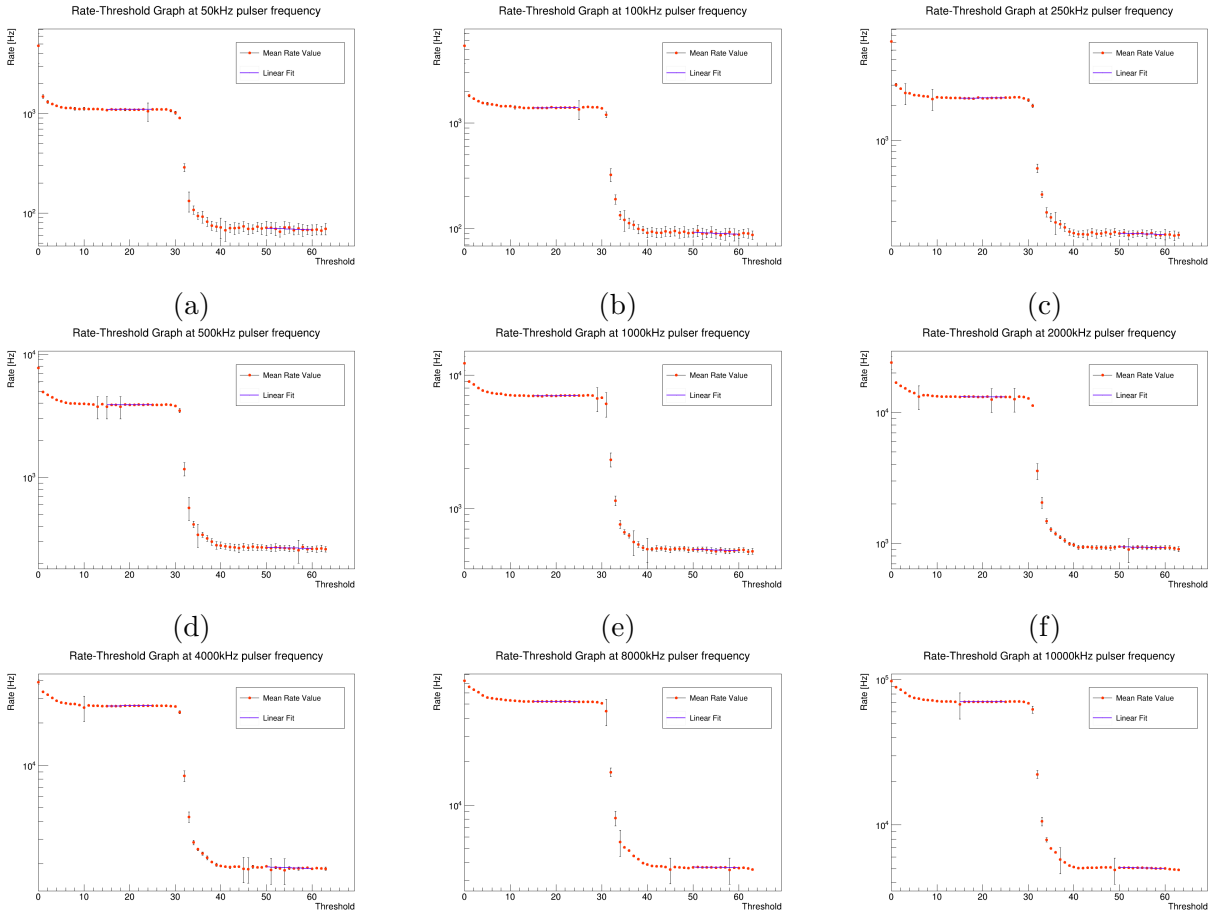

Figure 3.26: Distributions of mean measurements of photon detection rate from the reference A1 SiPM, as a function of the threshold voltage at which data acquisition is triggered, with laser on, at different pulser frequencies; a straight line is fitted in two ranges of the X-axis: 15÷25 and 50÷60.

3.3.8 Faraday cage for the laser

At last, the ALPHALAS diode laser has been covered in a layer of tinfoil (Figure 3.27). This cover acts as a Faraday cage around the device, limiting the spread of noise signals that would inevitably affect measurements from SiPM sensors. This operation is useful in SiPMs' output signal analyses: the less background noise, the most precise the rising edge of the signal will be, allowing for more precise and reliable time-resolution measurements, as reported in Section 3.4.

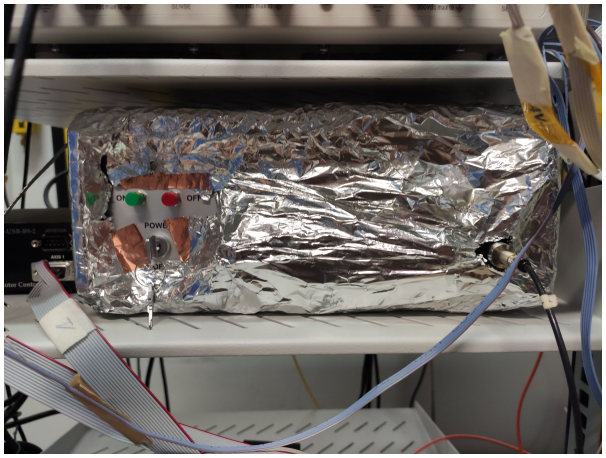

Figure 3.27: Diode laser covered in tinfoil; knobs, buttons and input terminal made accessible through express apertures in the tinfoil layer.

3.4 Final system characterization

The produced set-up has then been used for R&D for the EIC project, specifically for time-resolution measurements. Figure 3.28 shows a schematic of the measurement setup.

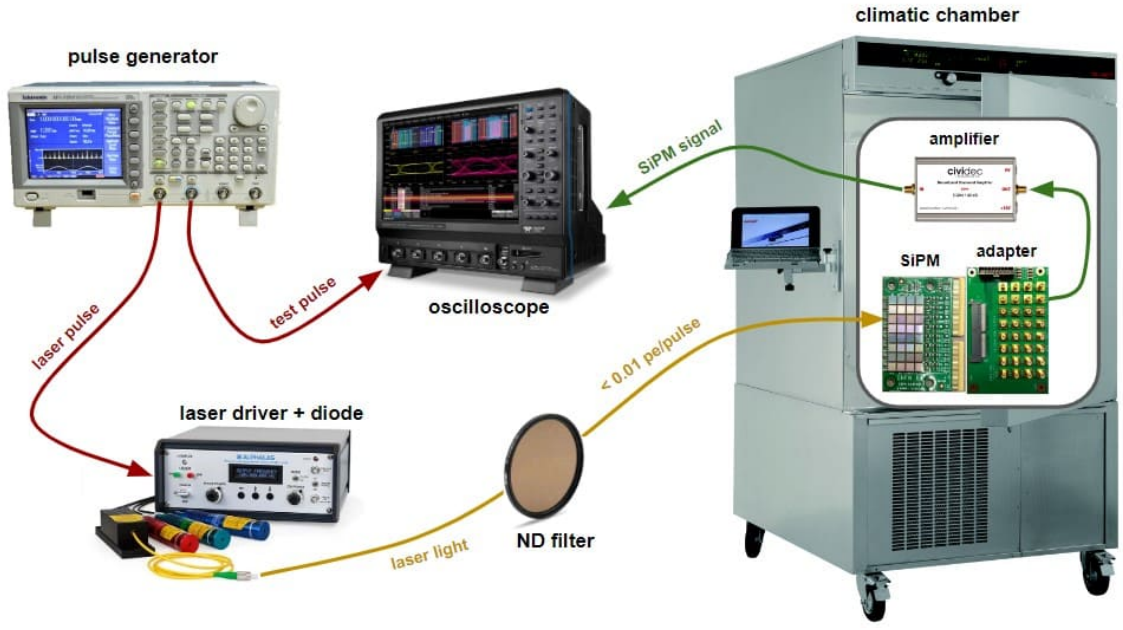

Figure 3.28: Diagram of the setup for timing measurements.

Keeping the reference SiPM at a temperature of -30 °C, it has been lit by the laser,

operated using the Tektronix function generator. Then, the Lecroy Waverunner 40186 oscilloscope has been used to analyze the time distance Δt between the rising edge of the pulsed signal that is sent to the laser and the rising edge of the output signal from the reference SiPM, as Figure 3.29 (left) shows. Δt is measured from 50% of the lase pulse rising edge to 50% of the SiPM pulse rising edge.
Δt undergoes random fluctuations by a certain quantity we refer to as σ. When the tested sensor operates at $V_{bias} = 55$ V, the oscilloscope measures $\sigma \sim 60$ ps. This latter measurement gets a contribution from the jitter that affects synchronization between the laser and the oscilloscpe, that is $\sigma_{sync} \sim 30$ ps, that is totally equivalent to j_1 reported in Paragraph 3.2.2. We can then compute the square-difference between the total 60 ps jitter and the 30 ps contribute, getting a new $\sigma = \sqrt{(60\ ps)^2 - (30\ ps)^2} \approx 52\ ps$, that is of the same order of magnitude as the σ reported in Figure 3.29 (right) and Figure 3.30.

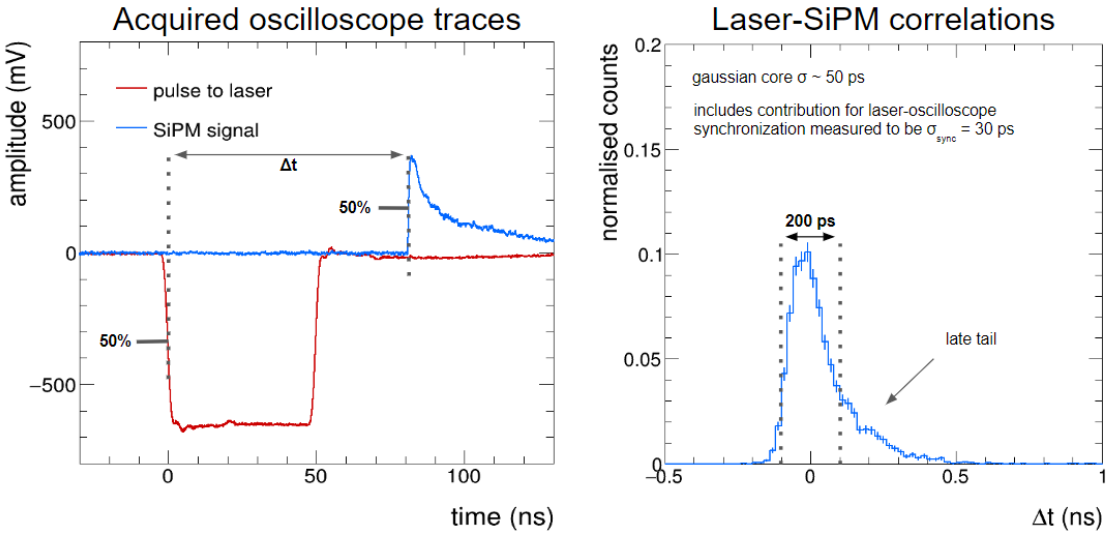

Figure 3.29: Profile of pulse signals, from both the function generator (that activates the laser) and the reference A1 SiPM, as a function of time (left); normalised photon count from the reference A1 SiPM as a function of Δt (right); both graphs report data for operating voltage $V_{bias} = 55$ V.

Figure 3.29 (right) shows the distribution of detected-photon counts from the reference SiPM as a function of Δt. The profile of the distribution is compatible with a gaussian form, with an exponential late tail. The origin of this late tail is not understood yet, but it is likely to be SiPM intrinsic. The same graph also highlights the curve's full width at half maximum, that depends on the operating voltage V_{bias} of the sensors and, in this case, it is smaller than 200 ps.
Figure 3.30 shows full width at half maximum (FWHM) for distributions analogous to that in Figure 3.29 (right), this time for different values of V_{bias}. It is noticeable how, for

$V_{bias} = 55$ V, FWHM measured via oscilloscope is close to 140 ps, if we take into account σ_{sync} previously mentioned, or 120 ps if we subtract σ_{sync}.
The ALPHALAS laser data sheet reports that, for a single laser pulse, full width at half maximum measure is FWHM $\sim$ 20 ps. This latter measure is smaller than any of the FWHM values reported in Figure 3.30, which are instead all above 120 ps (if we subtract σ_{sync}). Therefore, the laser device does not represent a limitation for time-resolution measurements in our system.

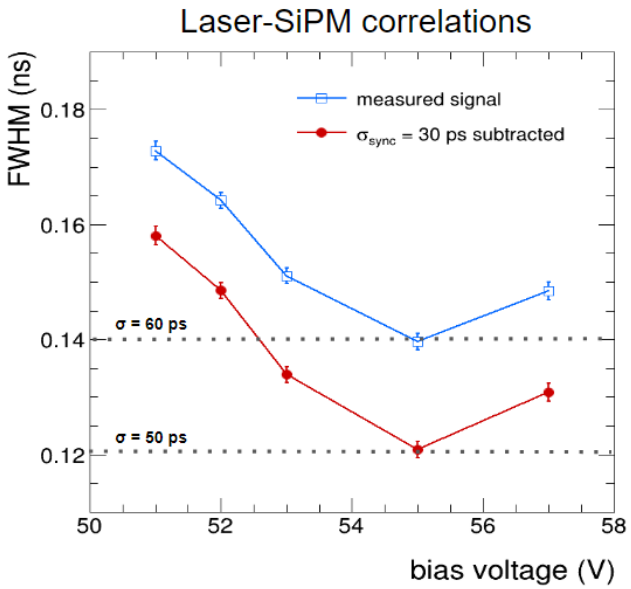

Figure 3.30: Full Width at Half Maximum (FWHM) as a function of the bias voltage of the reference SiPM.

Conclusions

The dRICH detector at the EIC will integrate SiPM sensors for particle identification. This thesis work reports the preparation, commissioning and characterization of an experimental set-up for the study of SiPM sensors.

A picosecond pulser laser system has been brought into operation. The setup includes: a picosecond diode laser, driven by an external pulse generator; a system of optical fibers and filters in order to manage the intensity of laser light on the SiPMs; a climatic chamber that keeps the sensors at temperature T = -30 °C, limiting thermal noise.
Analysis on average laser pulse power shows it increases non-linearly with respect to the laser pulse rate. Therefore, the performance of the system does depend on the laser pulse rate.
Characterisation studies of the system after tuning have shown that it was successfully configured to be utilised for SiPM characterisation in the single-photon regime. Detailed measurements show that crosstalk probability is about 6%, while the measured contamination from events with more than one delivered photon is lower than 0.1% for each laser pulse. Therefore, the laser system is capable of successfully delivering single-photon pulses with a negligible contribution of multi-photon events.

Finally, the system has been commissioned and used to measure the single-photon time-resolution of SiPM sensors. A preliminary analysis via oscilloscope shows that the picosecond laser does not represent a limitation for time-resolution measurements. In fact, from a reference SiPM, the full width at half maximum for a single-photon signal has been measured to be FWHM $\sim$ 120 ps, while for a laser pulse FWHM $\sim$ 20 ps, that is smaller in comparison.

Bibliography

[1] A. Accardi et al., "Electron Ion Collider: The Next QCD Frontier - Understanding the glue that binds us all", 2012. https://arxiv.org/pdf/1212.1701.pdf.

[2] R. Abdul Khalek et al., "Science Requirements and Detector Concepts for the Electron-Ion Collider: EIC Yellow Report", 2021. https://arxiv.org/pdf/2103.05419.pdf.

[3] J. Adam et al., "ATHENA detector proposal - a totally hermetic electron nucleus apparatus proposed for IP6 at the Electron-Ion Collider", 2022. https://arxiv.org/pdf/2210.09048.pdf.

[4] B.I. Shklovskii, A.L. Efros, "Electronic Properties of Doped Semiconductors", Springer-Verlag Berlin Heidelberg, 1984.

[5] A. Ghassemi, K. Sato, K. Kobayashi, "A technical guide to silicon photomultipliers (MPPC)", 2021. https://hub.hamamatsu.com/us/en/technical-notes/mppc-sipms.html.

[6] SensL, "An Introduction to the Silicon Photomultiplier". https://elearning.unimib.it/pluginfile.php/641517/mod_folder/content/0/Articoli/SiPM.pdf.

[7] E. Garutti, Yu. Musienko, "Radiation damage of SiPMs", 2018. https://arxiv.org/pdf/1809.06361.pdf.

[8] S. Gundacker and A. Heering, "The silicon photomultiplier: fundamentals and applications of a modern solid-state photon detector", *Phys. Med. Biol.*, vol. 65, 2020. https://doi.org/10.1088/1361-6560/ab7b2d.

[9] C. Piemonte and A. Gola, "Overview on the main parameters and technology of modern Silicon Photomultipliers" *Nuclear Instruments and Methods in Physics Research Section A: Accelerators, Spectrometers, Detectors and Associated Equipment*, 2019. https://www.sciencedirect.com/science/article/pii/S0168900218317716.

[10] R. Kugathasan, "A low-power mixed-signal ASIC for readout of SiPM at cryogenic temperature", 2019. https://pos.sissa.it/370/011/pdf.

[11] G. Fazzino, "Study of a pulsed LED set-up to characterise the light response of SiPM sensors for the EIC dRICH detector", bachelor thesis at Unibo, 2021/2022.

[12] M. Cordelli, E. Diociaiuti, A. Ferrari, S. Miscetti, S. Mueller, G. Pezzullo, I. Sarra, "An induced annealing technique for SiPMs neutron radiation damage," Journal of Instrumentation, 2021. https://iopscience.iop.org/article/10.1088/1748-0221/16/12/T12012/pdf.

[13] T. Tsang, T. Rao, S. Stoll, and C. Woody, "Neutron radiation damage and recovery studies of SiPMs," Journal of Instrumentation, 2016. https://iopscience.iop.org/article/10.1088/1748-0221/11/12/P12002/pdf.

[14] Shinya Hasuo, Tadahiro Ohmi, "Spatial Distribution of the Light Intensity in the Injection Lasers", *Jpn. J. Appl. Phys*, 1974. https://iopscience.iop.org/article/10.1143/JJAP.13.1429/pdf.

[15] Hira Nasim, Yasir Jamil, "Diode lasers: From laboratory to industry", 2014. https://www.sciencedirect.com/science/article/pii/S0030399213003010.

[16] Jun Xu, Joel Pokorny, Vivianne C. Smith, "Optical density of the human lens", 1997. https://opg.optica.org/view_article.cfm?pdfKey=9f50bf6b-9d62-4924-b16925274b03c063_1780https://opg.optica.org/view_article.cfm?pdfKey=9f50bf6b-9d62-4924-b16925274b03c063_1780.

[17] Pedro J. Aphalo, "Neutral density filters:theory vs. reality", 1997. http://www.bulletin.uv4plants.org/index.php/uv4pbulletin/article/view/uv4pb-2019-1-15.

[18] M. Rolo and F. Cossio, "The ALCOR ASIC for EIC applications", 2021. https://agenda.infn.it/event/28762/contributions/146408/attachments/87284/116576/20211121_ALCOR4EIC.pdf.

Ringraziamenti

Alle figure professionali che in primo luogo mi hanno accompagnato durante questo lavoro di tesi.
Ringrazio la prof.ssa Gilda Scioli, la cui figura di insegnante è stata per me un punto di riferimento, trasmettendo entusiasmo e fiducia nell'ultimo anno al corso di Fisica e nella cui figura di relatrice ho trovato attenzione, disponibilità e, di nuovo, entusiasmo, contagioso e produttivo.
Ringrazio il dottor Roberto Preghenella, con il quale ho trovato un ambiente tanto professionale, quanto energico e coinvolgente nel laboratorio di Berti Pichat, sempre seguito in un progetto di cui mi sono sentito parte e di cui ho apprezzato ogni sviluppo, anche al di fuori di questo lavoro di tesi.
Ringrazio Marco e Luigi per la disponibilità, i consigli, la presenza e l'aiuto durante le giornate in laboratorio.